1.3 Numerical Simulation of Marangoni Convection in Consideration of Free Surface Displacement (Part 6)

Hiroshi Kawamura

Science University of Tokyo

NUMERICAL SIMULATION OF MARANGONI CONVECTION IN CONSIDERATION OF FREE SURFACE DISPLACEMENT (PART 6)

Takanori Hashimoto*, Ichiro Ueno*, Hiroshi Kawamura* and Shinichi Yoda**

* Tokyo University of Science, 2641 Yamazaki, Noda-shi, Chiba 278-8510, Japan

** National Space Development Agency of Japan, 2-1-1 Sengen, Tsukuba City, 305-8505,Japan

Thermocapillary-driven convection in a half-zone liquid bridge has been extensively examined. A large number of researches have been conducted concerning the transition of the flow field. Physical mechanism of the transition, however, has not been fully understood. In the present study, three-dimensional numerical simulations taking with and without dynamic free surface deformation (DSD) into account are carried out to evaluate the effect of the surface deformation upon the flow field. The surface shape is solved by considering the stress balance on the free surface, and the calculation coordinate is reconstructed at every time step with employing a boundary fitted coordinate. The test fluids are acetone (Pr=4.38) and 2cSt silicone oil (Pr=28.11). The free surface deformation is determined primarily by the pressure variation. For acetone, the effect of the DSD upon critical point and flow field is quite small in the range of present numerical simulation. Mutual relation among the DSD, temperature, pressure and axial velocity is obtained.

1 INTRODUCTION

One of the purposes of the space environment utilization is the processing of a new material, because the buoyancy effect can be reduced in the space environment. Floating-zone method is one of the well-known material processing methods under the micro-gravity. In this method, however, the convective motion still occurs induced by the surface tension difference on the free surface owing to the temperature gradient. This convection is called thermocapillary or Marangoni convection, and has been widely investigated with a half-zone (HZ) model corresponding to half part of floating-zone model. In the HZ model, a liquid bridge is sustained between the coaxial cylindrical rods. Each rod is maintained at different temperature, thus the liquid bridge is exposed by a temperature difference ΔT between the both rods. When ΔT exceeds a critical value ΔT_c, the induced flow in the HZ bridge of medium and high Prandtl number fluid exhibits a transition from a two-dimensional steady flow to a three-dimensional oscillatory one. The oscillatory flow has two patterns called as 'Standing wave' and 'Traveling wave'. These flows appear depending upon the temperature

difference. The structure in the liquid bridge is characterized further by the azimuthal wave number m. The flow field is divided azimuthally into 2×m sectors; the alternate sector, m in total, consists of the same thermal-fluid structure.

The experiments for the thermocapillary convection have been widely conducted. Preisser et al. (1983) [1] investigated the oscillatory flow to study the effect of several parameters such as the aspect ratio and Marangoni number. Velten et al. (1991) [2] observed the periodic instability of thermocapillary convection in the cylindrical liquid bridge.

As for the numerical simulation, Kuhlmann (1993)[3] and Wanschura et al. (1995)[4] calculated the critical Reynolds number for the various non-dimensional numbers (Bi, Gr, Pr, A) using the linear stability analysis. Savino and Monti (1996) [5] simulated the oscillatory flow numerically and compared it with their experiments. Shevtsova et al. (1998) [6] studied the transition from two dimensional thermoconvective steady flow to a time-dependent flow considered for an axisymmetric liquid bridge of a high Prandtl number fluid (Pr = 105) with a static curved free surface.

It should be noted that most of the existing numerical simulations were conducted without considering the dynamic free surface deformation (DSD). After the onset of oscillation, however, the pressure field fluctuates violently because of the unsteady flow. Therefore the free surface is expected to dynamically deform due to these fluctuation. In fact, the free surface vibration in the liquid bridge has been observed in some terrestrial experiments. Kamotani et al. (2000) [7] reported an experiment of the thermocapillary convection performed aboard the Spacelab in an open cylindrical container, and investigated the free surface movement. In addition, they analyzed the influence of surface deformation upon the critical condition in the half-zone configuration. Correlation between the criticality and the dynamic surface deformation, however, is not understood yet. An influence of surface vibration upon the flow field instability must be evaluated to understand the mechanism of the oscillatory flow. To the authors' knowledge, no numerical works have been done on the thermocapillary convection in a liquid bridge with including the dynamic deformation of the surface.

Recently, Kuhlmann et al. [8] have made a combined analytical and numerical study on the thermocapillary convection in a liquid bridge with including the DSD using the linear stability analysis. They analyzed the mutual relation between the flow field and the dynamic surface deformation in the most dangerous mode. The present study aims at understanding time-dependent thermal-fluid phenomena with dynamic free surface deformation in the half-zone liquid bridge by a direct nonlinear numerical simulation.

2 NOMENCLATURES

Γ	aspect ratio
D	diameter
g	gravity
h	heat transfer coefficient
H	height of the liquid bridge
I	unit matrix
J	Jacobian
m	azimuthal wave number
n	surface-normal vector
N	normalizing dominator
P	pressure
$r,\ \theta, z$	coordinates
ξ, ζ, η	coordinates in the computational domain
R, R_k	position of the free surface
R_0	radius of the disk
$R_{1,2}$	main radii of curvature
S	stress tensor
t	time
T	temperature
T_0	reference temperature
U_0	maximum velocity
$V_{r,\theta,z}, V_{x,y}$	velocities
v_i	compensated temporally velocity
v_i	temporally velocity
V	volume of the liquid bridge
$V_{\xi,\zeta,\eta}$	contravariant velocities
$V_{\xi,\zeta,\eta}$	temporally contravariant velocities
α	contact angle
β	thermal expansion coefficient
ΔT	temperature difference between the disks
δ_s	amount of free surface deformation
τ	time in the computational domain
$\sigma,\ \sigma(T)$	surface tension
$\sigma(T_0)$	reference surface tension
σ_T	thermal coefficient of surface tension
κ	thermal diffusivity
λ	thermal conductivity
μ	dynamic viscosity
ν	kinematic viscosity
ρ	density
Bi	Biot number
Bo	Bond number
Ca	Capillary number
Gr	Grashof number
Ma	Marangoni number
Pr	Prandtl number
Re	Reynolds number

3 NUMERICAL METHOD

The purpose of this study is to analyze the influence of the free surface deformation upon the thermocapillary flow. Therefore, a numerical method to capture the temporally varying surface motion is employed. The deformed surface is expressed using the boundary fitted coordinate (BFC).

To consider the thermocapillary convection in a liquid bridge, a configuration of the analysis is defined as shown in Fig. 1. The liquid bridge with volume V_0 is sustained by two rigid parallel disks of equal radii $r = R_0$ located at $z = 0$ and H. The temperature difference between these disks is defined by ΔT.

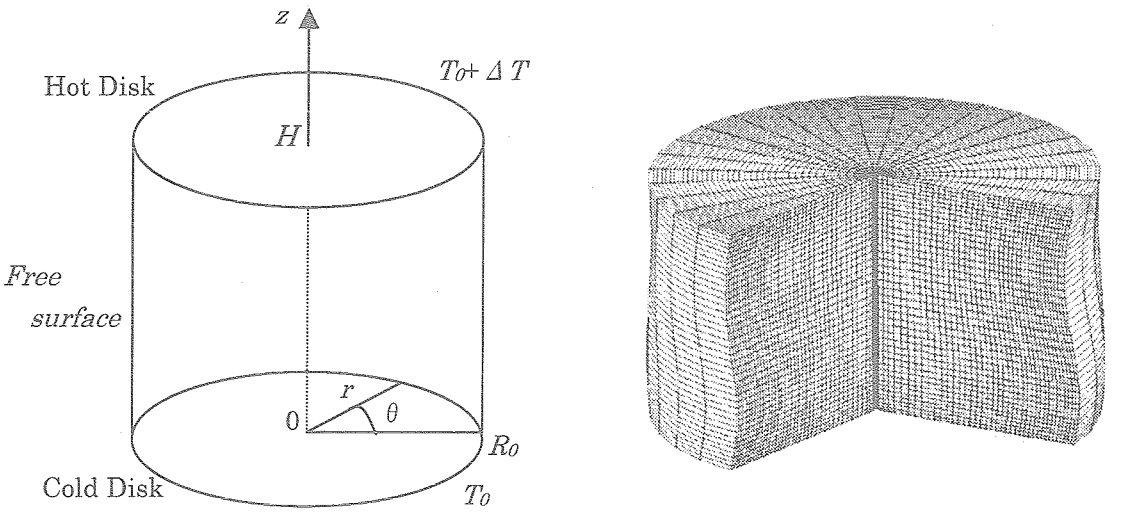

Figure 1: Numerical configuration

3.1 Governing equations

The liquid is assumed to be an incompressible Newtonian fluid of kinematic viscosity ν and density ρ. In a cylindrical coordinate system, the continuity, the Navier-Stokes and the energy equations are given by

$$\nabla \cdot \mathbf{u} = 0 \tag{1}$$

$$\frac{\partial \mathbf{u}}{\partial t} + (\mathbf{u} \cdot \nabla)\mathbf{u} = -\nabla P + \frac{Pr}{Ma}\nabla^2 \mathbf{u} \tag{2}$$

$$\frac{\partial T}{\partial t} + (\mathbf{u} \cdot \nabla)T = \frac{1}{Ma}\nabla^2 T \tag{3}$$

Variables are non-dimensionalized using scales shown in Table 1.

Table 1: Scales used for non-dimensionalization

Variable	r, z	t	$v=(v_r, v_\theta, v_z)$	p	T
Scale	H	$H\mu / \sigma_T \Delta T$	$\sigma_T \Delta T / \rho \nu$	$\rho(\sigma_T \Delta T/\mu)^2$	ΔT

The non-dimensional numbers are defined by

$$Re = \frac{U_0 H}{\nu}$$

$$Pr = \frac{\nu}{\kappa}$$

$$Ma = \frac{1}{\mu\kappa}\left|\frac{\partial\sigma}{\partial T}\right|\Delta T \cdot H$$

3. 2 Boundary fitted coordinate

The shape of the liquid bridge is deformed dynamically in this calculation. Therefore, the adequate coordinate system must be employed to calculate the flow field with the finite difference method. The boundary fitted coordinate method is applied to the governing equations in all directions. In the previous study, the computational domain was assumed to be cubic. The substantial error arises in the conversion from the cylinder in the physical domain to the cubic in the computational one. Thus, the present computational domain is modified to cylindrical coordinate. Equations (1)-(3) can be transformed from the physical domain to the computational domain by Jacobian matrix.

$$\begin{bmatrix} \frac{\partial}{\partial t} \\ \frac{\partial}{\partial r} \\ \frac{\partial}{\partial \theta} \\ \frac{\partial}{\partial z} \end{bmatrix} = \begin{bmatrix} 1 & \xi_t & \zeta_t & \eta_t \\ 0 & \xi_r & \zeta_r & \eta_r \\ 0 & \xi_\theta & \zeta_\theta & \eta_\theta \\ 0 & \xi_z & \zeta_z & \eta_z \end{bmatrix} \begin{bmatrix} \frac{\partial}{\partial \tau} \\ \frac{\partial}{\partial \xi} \\ \frac{\partial}{\partial \zeta} \\ \frac{\partial}{\partial \eta} \end{bmatrix} \tag{4}$$

$$\begin{bmatrix} \frac{\partial}{\partial \tau} \\ \frac{\partial}{\partial \xi} \\ \frac{\partial}{\partial \zeta} \\ \frac{\partial}{\partial \eta} \end{bmatrix} = \begin{bmatrix} 1 & r_\tau & \theta_\tau & z_\tau \\ 0 & r_\xi & \theta_\xi & z_\xi \\ 0 & r_\zeta & \theta_\zeta & z_\zeta \\ 0 & r_\eta & \theta_\eta & z_\eta \end{bmatrix} \begin{bmatrix} \frac{\partial}{\partial t} \\ \frac{\partial}{\partial r} \\ \frac{\partial}{\partial \theta} \\ \frac{\partial}{\partial z} \end{bmatrix} \tag{5}$$

Equation (5) is inversely transformed as follows,

$$\begin{bmatrix} \frac{\partial}{\partial t} \\ \frac{\partial}{\partial r} \\ \frac{1}{r}\frac{\partial}{\partial \theta} \\ \frac{\partial}{\partial z} \end{bmatrix} = \frac{1}{J}\begin{bmatrix} A_{11} & A_{12} & A_{13} & A_{14} \\ A_{21} & A_{22} & A_{23} & A_{24} \\ A_{31} & A_{32} & A_{33} & A_{34} \\ A_{41} & A_{42} & A_{43} & A_{44} \end{bmatrix}\begin{bmatrix} \frac{\partial}{\partial \tau} \\ \frac{\partial}{\partial \xi} \\ \frac{1}{\xi}\frac{\partial}{\partial \zeta} \\ \frac{\partial}{\partial \eta} \end{bmatrix} \tag{6}$$

where,

$$A_{11} = \frac{r}{\xi}\left(r_\xi\theta_\zeta z_\eta + r_\zeta\theta_\eta z_\xi + r_\eta\theta_\xi z_\zeta - r_\eta\theta_\zeta z_\xi - r_\zeta\theta_\xi z_\eta - r_\xi\theta_\eta z_\zeta\right),$$

$$A_{12} = -\frac{r}{\xi}\left(r_\tau\theta_\zeta z_\eta + r_\zeta\theta_\eta z_\tau + r_\eta\theta_\tau z_\zeta - r_\eta\theta_\zeta z_\tau - r_\zeta\theta_\tau z_\eta - r_\tau\theta_\eta z_\zeta\right),$$

$$A_{13} = r\left(r_\tau\theta_\xi z_\eta + r_\xi\theta_\eta z_\tau + r_\eta\theta_\tau z_\xi - r_\eta\theta_\xi z_\tau - r_\xi\theta_\tau z_\eta - r_\tau\theta_\eta z_\xi\right),$$

$$A_{14} = -\frac{r}{\xi}\left(r_\tau\theta_\xi z_\zeta + r_\xi\theta_\zeta z_\tau + r_\zeta\theta_\tau z_\xi - r_\zeta\theta_\xi z_\tau - r_\xi\theta_\tau z_\zeta - r_\tau\theta_\zeta z_\xi\right),$$

$$A_{21} = 0 \quad A_{22} = \frac{r}{\xi}\left(\theta_\zeta z_\eta - \theta_\eta z_\zeta\right), \quad A_{23} = -r\left(\theta_\xi z_\eta - \theta_\eta z_\xi\right), \quad A_{24} = \frac{r}{\xi}\left(\theta_\xi z_\zeta - \theta_\zeta z_\xi\right),$$

$$A_{31} = 0 \quad A_{32} = -\frac{1}{\xi}\left(r_\zeta z_\eta - r_\eta z_\zeta\right), \quad A_{33} = \left(r_\xi z_\eta - r_\eta z_\xi\right), \quad A_{34} = -\frac{1}{\xi}\left(r_\xi z_\zeta - r_\zeta z_\xi\right),$$

$$A_{41} = 0 \quad A_{42} = \frac{r}{\xi}\left(r_\zeta\theta_\eta - r_\eta\theta_\zeta\right), \quad A_{43} = -r\left(r_\xi\theta_\eta - r_\eta\theta_\xi\right), \quad A_{44} = \frac{r}{\xi}\left(r_\xi\theta_\zeta - r_\zeta\theta_\xi\right).$$

Each component can be related from Eqs. (4) and (6) as:

$$J = \frac{r}{\xi}\left(r_\xi\theta_\zeta z_\eta + r_\zeta\theta_\eta z_\xi + r_\eta\theta_\xi z_\zeta - r_\eta\theta_\zeta z_\xi - r_\zeta\theta_\xi z_\eta - r_\xi\theta_\eta z_\zeta\right),$$

$$\xi_t = -\frac{1}{J}\frac{r}{\xi}\left(r_\tau\theta_\zeta z_\eta + r_\zeta\theta_\eta z_\tau + r_\eta\theta_\tau z_\zeta - r_\eta\theta_\zeta z_\tau - r_\zeta\theta_\tau z_\eta - r_\tau\theta_\eta z_\zeta\right),$$

$$\zeta_t = \frac{1}{J}r\left(r_\tau\theta_\xi z_\eta + r_\xi\theta_\eta z_\tau + r_\eta\theta_\tau z_\xi - r_\eta\theta_\xi z_\tau - r_\xi\theta_\tau z_\eta - r_\tau\theta_\eta z_\xi\right),$$

$$\eta_t = -\frac{1}{J}\frac{r}{\xi}\left(r_\tau\theta_\xi z_\zeta + r_\xi\theta_\zeta z_\tau + r_\zeta\theta_\tau z_\xi - r_\zeta\theta_\xi z_\tau - r_\xi\theta_\tau z_\zeta - r_\tau\theta_\zeta z_\xi\right),$$

$$\xi_r = \frac{1}{J}\frac{r}{\xi}\left(\theta_\zeta z_\eta - \theta_\eta z_\zeta\right), \quad \zeta_r = -\frac{1}{J}r\left(\theta_\xi z_\eta - \theta_\eta z_\xi\right), \quad \eta_r = \frac{1}{J}\frac{r}{\xi}\left(\theta_\xi z_\zeta - \theta_\zeta z_\xi\right),$$

$$\xi_\theta = -\frac{1}{J}\frac{1}{\xi}\left(r_\zeta z_\eta - r_\eta z_\zeta\right), \quad \zeta_\theta = \frac{1}{J}\left(r_\xi z_\eta - r_\eta z_\xi\right), \quad \eta_\theta = -\frac{1}{J}\frac{1}{\xi}\left(r_\xi z_\zeta - r_\zeta z_\xi\right),$$

$$\xi_z = \frac{1}{J}\frac{r}{\xi}\left(r_\zeta\theta_\eta - r_\eta\theta_\zeta\right), \quad \zeta_z = -\frac{1}{J}r\left(r_\xi\theta_\eta - r_\eta\theta_\xi\right), \quad \eta_z = \frac{1}{J}\frac{r}{\xi}\left(r_\xi\theta_\zeta - r_\zeta\theta_\xi\right).$$

The continuity, the Navier- Stokes and the energy equations (Eqs. (1)-(3)) are transformed to the ones in the generalized coordinates.

[Continuity equation]

$$\frac{1}{\xi}\frac{\partial}{\partial\xi}\left(J\xi V_\xi\right)+\frac{1}{\xi}\frac{\partial}{\partial\zeta}\left(JV_\zeta\right)+\frac{\partial}{\partial\eta}\left(JV_\eta\right)=0 \tag{7}$$

where

$$V_\xi=\xi_r v_r+\frac{1}{r}\xi_\theta v_\theta+\xi_z v_z,\quad V_\zeta=\xi\zeta_r v_r+\frac{1}{r}\xi\zeta_\theta v_\theta+\xi\zeta_z v_z,\quad V_\eta=\eta_r v_r+\frac{1}{r}\eta_\theta v_\theta+\eta_z v_z.$$

These velocities are called as contravariant velocities.

[Navier-Stokes equation]

$$\begin{aligned}
&\frac{\partial v_i}{\partial t}+\xi_t\frac{\partial v_i}{\partial\xi}+\zeta_t\frac{\partial v_i}{\partial\zeta}+\eta_t\frac{\partial v_i}{\partial\eta}\\
&+\frac{1}{J}\left[\frac{1}{\xi}\frac{\partial}{\partial\xi}\left(J\xi V_\xi v_i\right)+\frac{1}{\xi}\frac{\partial}{\partial\zeta}\left(JV_\zeta v_i\right)+\frac{\partial}{\partial\eta}\left(JV_\eta v_i\right)+e_r\left(-\frac{Jv_\theta^2}{r}\right)+e_\theta\left(\frac{Jv_r v_\theta}{r}\right)\right]\\
&=-\left(\xi_i\frac{\partial P}{\partial\xi}+\zeta_i\frac{\partial P}{\partial\zeta}+\eta_i\frac{\partial P}{\partial\eta}\right)e_i\\
&+\frac{Pr}{Ma}\frac{1}{J}\left[\ \frac{1}{\xi}\frac{\partial}{\partial\xi}\left(J\xi\xi_r\xi_r\frac{\partial v_i}{\partial\xi}\right)+\frac{1}{\xi}\frac{\partial}{\partial\xi}\left(J\xi\xi_r\zeta_r\frac{\partial v_i}{\partial\zeta}\right)+\frac{1}{\xi}\frac{\partial}{\partial\xi}\left(J\xi\xi_r\eta_r\frac{\partial v_i}{\partial\eta}\right)\right.\\
&\quad+\frac{1}{\xi}\frac{\partial}{\partial\zeta}\left(J\xi\zeta_r\xi_r\frac{\partial v_i}{\partial\xi}\right)+\frac{\partial}{\partial\zeta}\left(J\xi\zeta_r\zeta_r\frac{\partial v_i}{\partial\zeta}\right)+\frac{\partial}{\partial\zeta}\left(J\xi\zeta_r\eta_r\frac{\partial v_i}{\partial\eta}\right)\\
&\quad+\frac{\partial}{\partial\eta}\left(J\eta_r\xi_r\frac{\partial v_i}{\partial\xi}\right)+\frac{\partial}{\partial\eta}\left(J\eta_r\zeta_r\frac{\partial v_i}{\partial\zeta}\right)+\frac{\partial}{\partial\eta}\left(J\eta_r\eta_r\frac{\partial v_i}{\partial\eta}\right)\\
&\quad+\frac{\partial}{\partial\xi}\left(J\frac{1}{r^2}\xi_\theta\xi_\theta\frac{\partial v_i}{\partial\xi}\right)+\frac{\partial}{\partial\xi}\left(J\frac{1}{r^2}\xi_\theta\zeta_\theta\frac{\partial v_i}{\partial\zeta}\right)+\frac{\partial}{\partial\xi}\left(J\frac{1}{r^2}\xi_\theta\eta_\theta\frac{\partial v_i}{\partial\eta}\right)\\
&\quad+\frac{1}{\xi}\frac{\partial}{\partial\zeta}\left(J\frac{\xi}{r^2}\zeta_\theta\xi_\theta\frac{\partial v_i}{\partial\xi}\right)+\frac{1}{\xi}\frac{\partial}{\partial\zeta}\left(J\frac{\xi}{r^2}\zeta_\theta\zeta_\theta\frac{\partial v_i}{\partial\zeta}\right)+\frac{1}{\xi}\frac{\partial}{\partial\zeta}\left(J\frac{\xi}{r^2}\zeta_\theta\eta_\theta\frac{\partial v_i}{\partial\eta}\right)\\
&\quad+\frac{\partial}{\partial\eta}\left(J\frac{1}{r^2}\eta_\theta\xi_\theta\frac{\partial v_i}{\partial\xi}\right)+\frac{\partial}{\partial\eta}\left(J\frac{1}{r^2}\eta_\theta\zeta_\theta\frac{\partial v_i}{\partial\zeta}\right)+\frac{\partial}{\partial\eta}\left(J\frac{1}{r^2}\eta_\theta\eta_\theta\frac{\partial v_i}{\partial\eta}\right)\\
&\quad+\frac{1}{\xi}\frac{\partial}{\partial\xi}\left(J\xi\xi_z\xi_z\frac{\partial v_i}{\partial\xi}\right)+\frac{\partial}{\partial\xi}\left(J\xi\xi_z\zeta_z\frac{\partial v_i}{\partial\zeta}\right)+\frac{\partial}{\partial\xi}\left(J\xi\xi_z\eta_z\frac{\partial v_i}{\partial\eta}\right)\\
&\quad+\left.\frac{1}{\xi}\frac{\partial}{\partial\zeta}\left(J\xi\zeta_z\xi_z\frac{\partial v_i}{\partial\xi}\right)+\frac{\partial}{\partial\zeta}\left(J\xi\zeta_z\zeta_z\frac{\partial v_i}{\partial\zeta}\right)+\frac{\partial}{\partial\zeta}\left(J\xi\zeta_z\eta_z\frac{\partial v_i}{\partial\eta}\right)\right.
\end{aligned}$$

$$
\begin{aligned}
&+ \frac{\partial}{\partial\eta}\left(J\eta_z\xi_z\frac{\partial v_i}{\partial\xi}\right)+\frac{\partial}{\partial\eta}\left(J\eta_z\zeta_z\frac{\partial v_i}{\partial\zeta}\right)+\frac{\partial}{\partial\eta}\left(J\eta_z\eta_z\frac{\partial v_i}{\partial\eta}\right)\\
&+ e_r\left(-J\frac{v_r}{r^2}-J\frac{2}{r^2}\left(\frac{1}{r}\xi_\theta\frac{\partial v_\theta}{\partial\xi}+\frac{1}{r}\zeta_\theta\frac{\partial v_\theta}{\partial\zeta}+\frac{1}{r}\eta_\theta\frac{\partial v_\theta}{\partial\eta}\right)\right)\\
&+ e_\theta\left(-J\frac{v_\theta}{r^2}-J\frac{2}{r^2}\left(\frac{1}{r}\xi_\theta\frac{\partial v_r}{\partial\xi}+\frac{1}{r}\zeta_\theta\frac{\partial v_r}{\partial\zeta}+\frac{1}{r}\eta_\theta\frac{\partial v_r}{\partial\eta}\right)\right)\ \Bigg]\\
&+ e_z\left(\frac{Gr}{Re^2}T\right)
\end{aligned}
\tag{8}
$$

where, $v_i=(v_r,v_\theta,v_z)$.

[Energy equation]

$$
\begin{aligned}
&\frac{\partial T}{\partial t}+\xi_t\frac{\partial T}{\partial\xi}+\zeta_t\frac{\partial vT}{\partial\zeta}+\eta_t\frac{\partial T}{\partial\eta}\\
&+\frac{1}{J}\left[\frac{1}{\xi}\frac{\partial}{\partial\xi}\left(J\xi V_\xi T\right)+\frac{1}{\xi}\frac{\partial}{\partial\zeta}\left(JV_\zeta T\right)+\frac{\partial}{\partial\eta}\left(JV_\eta T\right)\right]
\end{aligned}
$$

$$
\begin{aligned}
=\frac{1}{Ma}\frac{1}{J}\Bigg[\ &\frac{1}{\xi}\frac{\partial}{\partial\xi}\left(J\xi\xi_r\xi_r\frac{\partial T}{\partial\xi}\right)+\frac{1}{\xi}\frac{\partial}{\partial\xi}\left(J\xi\xi_r\zeta_r\frac{\partial T}{\partial\zeta}\right)+\frac{1}{\xi}\frac{\partial}{\partial\xi}\left(J\xi\xi_r\eta_r\frac{\partial T}{\partial\eta}\right)\\
&+\frac{1}{\xi}\frac{\partial}{\partial\zeta}\left(J\xi\zeta_r\xi_r\frac{\partial T}{\partial\xi}\right)+\frac{\partial}{\partial\zeta}\left(J\xi\zeta_r\zeta_r\frac{\partial T}{\partial\zeta}\right)+\frac{\partial}{\partial\zeta}\left(J\xi\zeta_r\eta_r\frac{\partial T}{\partial\eta}\right)\\
&+\frac{\partial}{\partial\eta}\left(J\eta_r\xi_r\frac{\partial T}{\partial\xi}\right)+\frac{\partial}{\partial\eta}\left(J\eta_r\zeta_r\frac{\partial T}{\partial\zeta}\right)+\frac{\partial}{\partial\eta}\left(J\eta_r\eta_r\frac{\partial T}{\partial\eta}\right)\\
&+\frac{\partial}{\partial\xi}\left(J\frac{1}{r^2}\xi_\theta\xi_\theta\frac{\partial T}{\partial\xi}\right)+\frac{\partial}{\partial\xi}\left(J\frac{1}{r^2}\xi_\theta\zeta_\theta\frac{\partial T}{\partial\zeta}\right)+\frac{\partial}{\partial\xi}\left(J\frac{1}{r^2}\xi_\theta\eta_\theta\frac{\partial T}{\partial\eta}\right)\\
&+\frac{1}{\xi}\frac{\partial}{\partial\zeta}\left(J\frac{\xi}{r^2}\zeta_\theta\xi_\theta\frac{\partial T}{\partial\xi}\right)+\frac{1}{\xi}\frac{\partial}{\partial\zeta}\left(J\frac{\xi}{r^2}\zeta_\theta\zeta_\theta\frac{\partial T}{\partial\zeta}\right)+\frac{1}{\xi}\frac{\partial}{\partial\zeta}\left(J\frac{\xi}{r^2}\zeta_\theta\eta_\theta\frac{\partial T}{\partial\eta}\right)\\
&+\frac{\partial}{\partial\eta}\left(J\frac{1}{r^2}\eta_\theta\xi_\theta\frac{\partial T}{\partial\xi}\right)+\frac{\partial}{\partial\eta}\left(J\frac{1}{r^2}\eta_\theta\zeta_\theta\frac{\partial T}{\partial\zeta}\right)+\frac{\partial}{\partial\eta}\left(J\frac{1}{r^2}\eta_\theta\eta_\theta\frac{\partial T}{\partial\eta}\right)\\
&+\frac{1}{\xi}\frac{\partial}{\partial\xi}\left(J\xi\xi_z\xi_z\frac{\partial T}{\partial\xi}\right)+\frac{\partial}{\partial\xi}\left(J\xi\xi_z\zeta_z\frac{\partial T}{\partial\zeta}\right)+\frac{\partial}{\partial\xi}\left(J\xi\xi_z\eta_z\frac{\partial T}{\partial\eta}\right)\\
&+\frac{1}{\xi}\frac{\partial}{\partial\zeta}\left(J\xi\zeta_z\xi_z\frac{\partial T}{\partial\xi}\right)+\frac{\partial}{\partial\zeta}\left(J\xi\zeta_z\zeta_z\frac{\partial T}{\partial\zeta}\right)+\frac{\partial}{\partial\zeta}\left(J\xi\zeta_z\eta_z\frac{\partial T}{\partial\eta}\right)\\
&+\frac{\partial}{\partial\eta}\left(J\eta_z\xi_z\frac{\partial T}{\partial\xi}\right)+\frac{\partial}{\partial\eta}\left(J\eta_z\zeta_z\frac{\partial T}{\partial\zeta}\right)+\frac{\partial}{\partial\eta}\left(J\eta_z\eta_z\frac{\partial T}{\partial\eta}\right)
\end{aligned}
\tag{9}
$$

In this analysis, fractional step method is utilized to solve these governing equations. Adams-Bashforth method is adapted for time advancement. The Crank-Nicholson scheme is applied only the circumferential constituent of the viscous terms in the Navier-Stokes and the energy equations in order to ensure a larger stability margin.

3.3 Boundary conditions

3.3.1 Boundary condition of the velocity

To derive the boundary condition of the velocity on the free surface, the balance between the shearing stress and the surface tension must be considered.

The relation between the shearing stress and the surface tension is shown in Fig. 2.

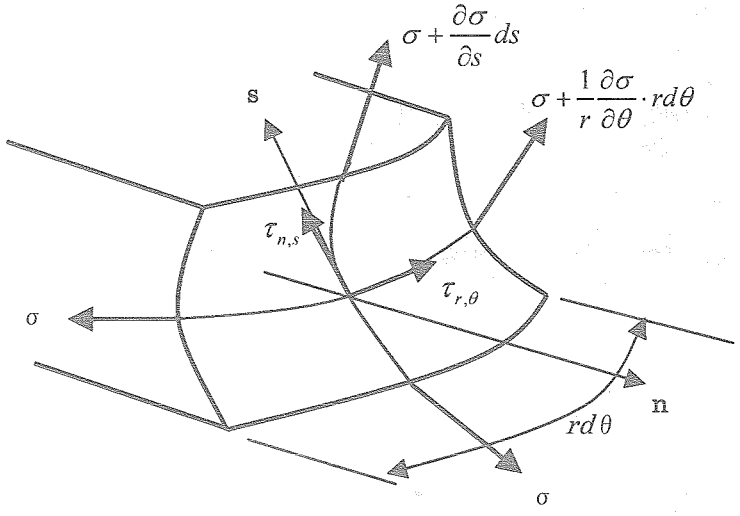

Figure 2: Stress balance between shearing stress and surface tension

From Fig. 2 the equations of the balance between the shearing stress and the surface tension are described as

$$\begin{cases} \tau_{n,s} \cdot rd\theta ds = \left\{ \left(\sigma + \dfrac{\partial \sigma}{\partial s} \cdot ds \right) - \sigma \right\} \cdot rd\theta \\ \tau_{r,\theta} \cdot rd\theta ds = \left\{ \left(\sigma + \dfrac{1}{r}\dfrac{\partial \sigma}{\partial \theta} \cdot rd\theta \right) - \sigma \right\} \cdot rds \end{cases} \tag{10}$$

Newton's law of viscosity is expressed as follows.

$$\begin{cases} \tau_{n,s} = \mu \left\{ \dfrac{\partial v_s}{\partial n} + \dfrac{\partial v_n}{\partial s} \right\} \\ \tau_{r,\theta} = \mu \left\{ \dfrac{1}{r}\dfrac{\partial v_r}{\partial \theta} + r\dfrac{\partial}{\partial r}\left(\dfrac{v_\theta}{r} \right) \right\} \end{cases} \tag{11}$$

From Eqs. (10) and (11), equation (12) is derived.

$$\begin{cases} \mu\left\{\dfrac{\partial v_s}{\partial n}+\dfrac{\partial v_n}{\partial s}\right\}=\dfrac{\partial \sigma}{\partial s} \\ \mu\left\{\dfrac{1}{r}\dfrac{\partial v_r}{\partial \theta}+r\dfrac{\partial}{\partial r}\left(\dfrac{v_\theta}{r}\right)\right\}=\dfrac{1}{r}\dfrac{\partial \sigma}{\partial \theta} \end{cases} \tag{12}$$

If the velocity on the free surface in the normal direction is assumed to be zero, equation (12) can be shown as follows.

$$\begin{cases} \mu\dfrac{\partial v_s}{\partial n}=\dfrac{\partial \sigma}{\partial s} \\ \mu\left\{\dfrac{1}{r}\dfrac{\partial v_r}{\partial \theta}+r\dfrac{\partial}{\partial r}\left(\dfrac{v_\theta}{r}\right)\right\}=\dfrac{1}{r}\dfrac{\partial \sigma}{\partial \theta} \end{cases} \tag{13}$$

Equation (11) can be non-dimensionalized as following equations.

$$\begin{cases} \dfrac{\partial v_s}{\partial n}=-\dfrac{\partial \sigma}{\partial s} \\ \dfrac{1}{r}\dfrac{\partial v_r}{\partial \theta}+r\dfrac{\partial}{\partial r}\left(\dfrac{v_\theta}{r}\right)=-\dfrac{1}{r}\dfrac{\partial \sigma}{\partial \theta} \end{cases} \tag{14}$$

In the equation of the relation between normal and tangential directions, the tangential velocity v_s is divided into radius and axial directions (See Fig. 3).

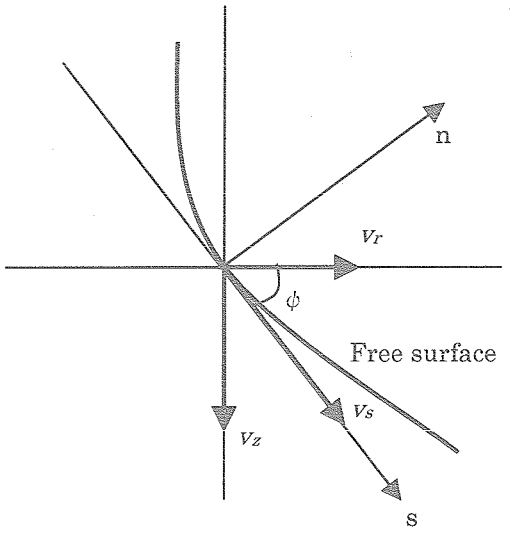

$$\begin{cases} v_r = v_s\cos\varphi \\ v_z = v_s\sin\varphi \end{cases} \tag{15}$$

$$\Leftrightarrow \begin{cases} v_s = \dfrac{v_r}{\cos\varphi} \\ v_s = \dfrac{v_z}{\sin\varphi} \end{cases} \tag{16}$$

$$\Leftrightarrow \begin{cases} \dfrac{\partial v_s}{\partial n}=\dfrac{\partial}{\partial n}\left(\dfrac{v_r}{\cos\varphi}\right) \\ \dfrac{\partial v_s}{\partial n}=-\dfrac{\partial}{\partial n}\left(\dfrac{v_z}{\sin\varphi}\right) \end{cases} \tag{17}$$

$$\Leftrightarrow \begin{cases} \dfrac{\partial}{\partial n}\left(\dfrac{v_r}{\cos\varphi}\right)=-\dfrac{\partial T}{\partial s} \\ \dfrac{\partial}{\partial n}\left(\dfrac{v_z}{\sin\varphi}\right)=-\dfrac{\partial T}{\partial s} \end{cases} \tag{18}$$

Figure 3: Velocity on the free surface

Generally the following relations are derived in the normal and tangential directions.

[Normal Derivatives]

$$\begin{cases} \dfrac{\partial \phi}{\partial n^{(\xi)}} = \dfrac{1}{J\sqrt{\alpha}}\left(\alpha\phi_{\xi} - \beta\phi_{\eta}\right) \\ \dfrac{\partial \phi}{\partial n^{(\eta)}} = \dfrac{1}{J\sqrt{\gamma}}\left(-\beta\phi_{\xi} + \gamma\phi_{\eta}\right) \end{cases} \tag{19}$$

[Tangential Derivatives]

$$\begin{cases} \dfrac{\partial \phi}{\partial s^{(\xi)}} = \dfrac{1}{\sqrt{\alpha}}\phi_{\eta} \\ \dfrac{\partial \phi}{\partial s^{(\eta)}} = \dfrac{1}{\sqrt{\gamma}}\phi_{\xi} \end{cases} \tag{20}$$

where, $\alpha = r_{\eta}^2 + z_{\eta}^2$, $\beta = r_{\xi}r_{\eta} + z_{\xi}z_{\eta}$, $\gamma = r_{\xi}^2 + z_{\xi}^2$.

Using eq. (19), the equation of the stress balance in normal and tangential directions is obtained.

$$\frac{1}{J\sqrt{\alpha}}\left(\alpha\frac{\partial v_z}{\partial \xi} - \beta\frac{\partial v_z}{\partial \eta}\right) = -sin\varphi\frac{1}{\sqrt{\alpha}}\frac{\partial T}{\partial \eta} \tag{21}.$$

The axial velocity is derived from eq. (21). The radial velocity is derived from the relation of following equation.

$$v_r = \frac{cos\varphi}{sin\varphi}v_z \tag{22}.$$

On the other hand, the boundary condition of the circumferential velocity is defined by

$$\frac{1}{r}\frac{\partial v_r}{\partial \theta} + r\frac{\partial}{\partial r}\left(\frac{v_{\theta}}{r}\right) = -\frac{1}{r}\frac{\partial T}{\partial \theta} \tag{23}.$$

Equation (23) is transformed to the one in the computational domain by the Jacobian matrix as

$$\begin{aligned} &\frac{1}{r}\left(\xi_{\theta}\frac{\partial v_r}{\partial \xi} + \zeta_{\theta}\frac{\partial v_r}{\partial \zeta} + \eta_{\theta}\frac{\partial v_r}{\partial \eta}\right) + r\left(\xi_r\frac{\partial}{\partial \xi}\left(\frac{v_{\theta}}{r}\right) + \zeta_r\frac{\partial}{\partial \zeta}\left(\frac{v_{\theta}}{r}\right) + \eta_r\frac{\partial}{\partial \eta}\left(\frac{v_{\theta}}{r}\right)\right) \\ &\quad = -\frac{1}{r}\left(\xi_{\theta}\frac{\partial T}{\partial \xi} + \zeta_{\theta}\frac{\partial T}{\partial \zeta} + \eta_{\theta}\frac{\partial T}{\partial \eta}\right) \end{aligned} \tag{24}.$$

3.3.2 Boundary condition of the temperature

The condition of the heat transfer over the free surface is assumed to be adiabatic. Therefore the equation of the boundary condition of the temperature is

$$\frac{\partial T}{\partial n} = 0 \tag{25}.$$

Equation (25) is transformed by equation (19) as

$$\frac{\partial T}{\partial n}=\frac{1}{J\sqrt{\alpha}}\left(\alpha\frac{\partial T}{\partial \xi}-\beta\frac{\partial T}{\partial \eta}\right) \tag{26}.$$

3.3.3 Treatment of the liquid center axis

In this analysis the governing equations are described in the cylindrical coordinate. Therefore the center of the cylinder (r = 0) can not be solved directly by the present equation. This problem is solved by a method described below. The computational grid is fixed at the center.

The Navier-Stokes equation in the axial direction and the energy equation at the center are derived by azimuthal integration.

[Navier-Stokes equation at the liquid center]

$$\begin{aligned}&r\frac{\partial v_z}{\partial t}+\frac{\partial}{\partial r}\left(rv_rv_z\right)+\frac{\partial}{\partial \theta}\left(v_\theta v_z\right)+\frac{\partial}{\partial z}\left(rv_zv_z\right)\\&=-r\frac{\partial P}{\partial z}+\frac{Pr}{Ma}\left[\frac{\partial}{\partial r}\left(r\frac{\partial v_z}{\partial r}\right)+\frac{\partial}{\partial \theta}\left(\frac{1}{r}\frac{\partial v_z}{\partial \theta}\right)+\frac{\partial}{\partial z}\left(r\frac{\partial v_z}{\partial z}\right)\right]\end{aligned}$$

$$\begin{aligned}\Rightarrow\ &\frac{\partial v_z}{\partial t}+\frac{\Delta\theta}{\pi\Delta r}\sum_{\theta=0}^{2\pi}\left(v_rv_z\right)+\frac{1}{\Delta z}\left[v_z^2\right]_0^{\Delta z}\\&=-\frac{\partial P}{\partial z}+\frac{Pr}{Ma}\left[\frac{\Delta\theta}{\pi\Delta r}\sum_{\theta=0}^{2\pi}\left.\frac{\partial v_z}{\partial r}\right|_{\Delta r}+\frac{1}{\Delta z}\left[\frac{\partial v_z}{\partial z}\right]_0^{\Delta z}\right]\end{aligned} \tag{27}$$

[Energy equation]

$$\begin{aligned}&r\frac{\partial T}{\partial t}+\frac{\partial}{\partial r}\left(rv_rT\right)+\frac{\partial}{\partial \theta}\left(v_\theta T\right)+\frac{\partial}{\partial z}\left(rv_zT\right)\\&=\frac{1}{Ma}\left[\frac{\partial}{\partial r}\left(r\frac{\partial T}{\partial r}\right)+\frac{\partial}{\partial \theta}\left(\frac{1}{r}\frac{\partial T}{\partial \theta}\right)+\frac{\partial}{\partial z}\left(r\frac{\partial T}{\partial z}\right)\right]\end{aligned}$$

$$\begin{aligned}\Rightarrow\ &r\frac{\partial T}{\partial t}+\frac{\Delta\theta}{\pi\Delta r}\sum_{\theta=0}^{2\pi}\left(v_rT\right)+\frac{1}{\Delta z}\left[v_zT\right]_0^{\Delta z}\\&=\frac{1}{Ma}\left\{\frac{\Delta\theta}{\pi\Delta r}\sum_{\theta=0}^{2\pi}\left.\frac{\partial T}{\partial r}\right|_{\Delta r}+\frac{1}{\Delta z}\left[\frac{\partial T}{\partial z}\right]_0^{\Delta z}\right\}\end{aligned} \tag{28}$$

As for the radius and circumference velocity at the center, the velocity is evaluated by summed value over the surrounding mesh points (See Fig.4).

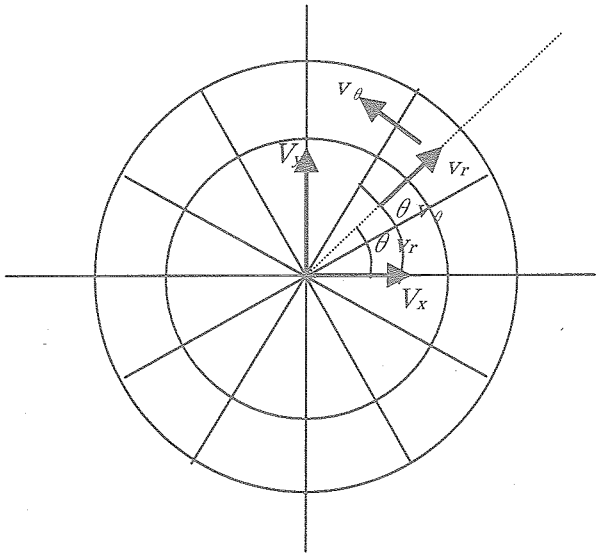

$$V_x = \sum_{\theta=0}^{2\pi}\left\{ v_r cos\theta_{v_r} + v_\theta cos\left(\theta_{v_\theta} + \frac{\pi}{2}\right)\right\}$$
$$V_y = \sum_{\theta=0}^{2\pi}\left\{ v_r sin\theta_{v_r} + v_\theta sin\left(\theta_{v_\theta} + \frac{\pi}{2}\right)\right\} \quad (29)$$

Figure 4: The velocity at the center axis

After the summation, the velocities V_x, V_y are divided into the radius and circumference components (v_r, v_θ) as follows;

$$v_r = \left[V_x cos\theta_{v_r} + V_y cos\left(\frac{\pi}{2} - \theta_{v_r}\right)\right]\frac{1}{nj}$$
$$v_\theta = \left[V_x\left(-sin\theta_{v_\theta}\right)cos + V_y sin\left(\frac{\pi}{2} - \theta_{v_\theta}\right)\right]\frac{1}{nj} \quad (30).$$

Here, nj shows the division number of the circumference direction. This treatment at the center axis is also applied to the energy equation.

3. 4 Free surface deformation

The stress balance over the free surface must be considered to compute the free surface shape. Along the interface between two immiscible fluids (1) and (2), the forces over the surface must be balanced. If the surface is plane and the surface tension is constant, the stress balance over the surface leads

$$\mathbb{S}^{(1)} \cdot \mathbf{n} = \mathbb{S}^{(2)} \cdot \mathbf{n} \quad (31)$$

where $\mathbb{S}$ is the stress tensor and $\mathbf{n}$ is the unit normal vector directed out of liquid (1) into the ambient fluid (2). The each component in the stress tensor is described as

$$S_{i,j} = -P\delta_{i,j} + \mu e_{i,j} \quad (32),$$

where $e_{i,j}$ can be expressed in the cylindrical coordinate as

$$e_{rr} = \frac{\partial v_r}{\partial r}, \quad e_{\theta\theta} = \frac{1}{r}\frac{\partial v_\theta}{\partial \theta} + \frac{v_r}{r}, \quad e_{zz} = \frac{\partial v_z}{\partial z},$$
$$e_{r\theta} = \frac{1}{2}\left\{ r\frac{\partial}{\partial r}\left(\frac{v_\theta}{r}\right) + \frac{1}{r}\frac{\partial v_r}{\partial \theta}\right\}, \quad e_{\theta z} = \frac{1}{2}\left\{\frac{1}{r}\frac{\partial v_z}{\partial \theta} + \frac{\partial v_\theta}{\partial z}\right\}, \quad e_{r\theta} = \frac{1}{2}\left\{\frac{\partial v_r}{\partial z} + \frac{\partial v_z}{\partial r}\right\} \quad (33).$$

On the other hand, if the free surface has curvature and the surface tension varies along the interface, the equation of the stress balance becomes [8]

$$\mathbb{S}^{(1)}\cdot\mathbf{n}+\sigma(\nabla\cdot\mathbf{n})\mathbf{n}-(\mathbf{I}-\mathbf{nn})\cdot\nabla\sigma=\mathbb{S}^{(2)}\cdot\mathbf{n} \tag{34}$$

where I is the identity matrix. The element $\sigma(\nabla\cdot\mathbf{n})$ in the second term in L. H. S. is so-called Laplace pressure. The mean curvatures of the interface,

$$\nabla\cdot\mathbf{n}=\frac{1}{R_1}+\frac{1}{R_2} \tag{35}$$

can be expressed as the sum of the inverse principle radii of curvatures R_1 and R_2. The mean curvatures of the interface can be described with Cartesian coordinate system as follows;

$$\begin{aligned}\nabla\cdot\mathbf{n}=\frac{-1}{R^3N^3}\Bigg[\quad & R\frac{\partial^2R}{\partial z^2}\left\{R^2+\left(\frac{\partial R}{\partial\theta}\right)^2\right\}\\ & +2\frac{\partial R}{\partial z}\frac{\partial R}{\partial\theta}\left(\frac{\partial R}{\partial z}\frac{\partial R}{\partial\theta}-R\frac{\partial^2R}{\partial z\partial\theta}\right)\\ & -\left\{1+\left(\frac{\partial R}{\partial z}\right)^2\right\}\left\{R^2+2\left(\frac{\partial R}{\partial\theta}\right)^2-R\frac{\partial^2R}{\partial\theta^2}\right\}\Bigg]\end{aligned} \tag{36}$$

where $N=\left[1+\left(\frac{\partial R}{\partial z}\right)^2+\frac{1}{R^2}\left(\frac{\partial R}{\partial\theta}\right)^2\right]^{\frac{1}{2}}$

The second term in the left hand side of equation (36) indicates the surface force acting tangentially originated from the surface tension σ. The operator I-nn represents the orthogonal projection of a vector onto the tangent plane defined by n.

Equation (34) can be non-dimensionalized using the scale as Table 1.

$$\mathbb{S}^{(1)}\cdot\mathbf{n}+\left(\frac{1}{Ca}-T\right)(\nabla\cdot\mathbf{n})\mathbf{n}-(\mathbf{I}-\mathbf{nn})\cdot\nabla T=\mathbb{S}^{(2)}\cdot\mathbf{n} \tag{37}$$

Here, the dimensionless parameter Ca is called as the Capillary number defined as

$$Ca=\frac{\sigma_T\Delta T}{\sigma_0} \tag{38}$$

From these equations, the equation of the stress balance is led in the three directions. Since the two directions of the curvature exist in the three dimension, the two tri-diagonal matrices must be considered for axial and circumferential directions. The tri-diagonal equations are indicated below.

[Radius direction]

$$\frac{\partial^2 R}{\partial z^2}=\frac{-R^3N^3}{R\left\{R^2+\left(\partial R/\partial\theta\right)^2\right\}\left(1/Ca-T\right)}\Bigg[\quad Re\left(P^{(1)}-P^{(2)}\right)-\frac{Bo}{Ca}\left(H-z\right)-\frac{\partial v_r}{\partial r}$$
$$-\frac{1}{2}\left\{r\frac{\partial}{\partial r}\left(\frac{v_\theta}{r}\right)+\frac{1}{r}\frac{\partial v_r}{\partial\theta}\right\}\frac{n_\theta}{n_r}-\frac{1}{2}\left(\frac{\partial v_r}{\partial z}+\frac{\partial v_z}{\partial r}\right)\frac{n_z}{n_r}$$
$$-\frac{1-n_r^2}{n_r}\frac{\partial T}{\partial r}+n_\theta\frac{1}{r}\frac{\partial T}{\partial\theta}+n_z\frac{\partial T}{\partial z}\Bigg]$$
$$+\frac{1}{R\left\{R^2+\left(\partial R/\partial\theta\right)^2\right\}}\Bigg[-2\frac{\partial R}{\partial z}\frac{\partial R}{\partial\theta}\left(\frac{\partial R}{\partial z}\frac{\partial R}{\partial\theta}-R\frac{\partial^2 R}{\partial z\partial\theta}\right)$$
$$+\left\{1+\left(\frac{\partial R}{\partial z}\right)^2\right\}\left\{R^2+2\left(\frac{\partial R}{\partial\theta}\right)^2-R\frac{\partial^2 R}{\partial\theta^2}\right\}\Bigg] \tag{39}$$

[Circumferential direction]

$$\frac{\partial^2 R}{\partial\theta^2}=\frac{-R^3N^3}{R\left\{R^2+\left(\partial R/\partial z\right)^2\right\}\left(1/Ca-T\right)}\Bigg[\quad Re\left(P^{(1)}-P^{(2)}\right)-\frac{Bo}{Ca}\left(H-z\right)-\frac{\partial v_r}{\partial r}$$
$$-\frac{1}{2}\left\{r\frac{\partial}{\partial r}\left(\frac{v_\theta}{r}\right)+\frac{1}{r}\frac{\partial v_r}{\partial\theta}\right\}\frac{n_\theta}{n_r}-\frac{1}{2}\left(\frac{\partial v_r}{\partial z}+\frac{\partial v_z}{\partial r}\right)\frac{n_z}{n_r}$$
$$-\frac{1-n_r^2}{n_r}\frac{\partial T}{\partial r}+n_\theta\frac{1}{r}\frac{\partial T}{\partial\theta}+n_z\frac{\partial T}{\partial z}\Bigg]$$
$$+\frac{1}{R\left\{R^2+\left(\partial R/\partial z\right)^2\right\}}\Bigg[-R\frac{\partial^2 R}{\partial z^2}\left\{R^2+\left(\frac{\partial R}{\partial\theta}\right)^2\right\}$$
$$-2\frac{\partial R}{\partial z}\frac{\partial R}{\partial\theta}\left(\frac{\partial R}{\partial z}\frac{\partial R}{\partial\theta}-R\frac{\partial^2 R}{\partial z\partial\theta}\right)\Bigg]$$
$$+\frac{2}{R}\left(\frac{\partial R}{\partial\theta}\right)^2+R \tag{40}$$

In addition to these tri-diagonal equations, the constant volume equation is solved to maintain the volume of the liquid bridge constant.

$$\int_0^H\int_0^{2\pi}\frac{1}{2}R^2\,d\theta\,dz=V \tag{41}$$

The position of the free surface R can be obtained by using Tri-Diagonal Matrix Algorithm (TDMA) in the axial and circumferential directions. [10]

4 RESULTS

4.1 Medium Pr fluid

We perform the simulation with Pr = 4.38 (acetone), aspect ratio $\Gamma(=H/R)$= 1.0 and volume ratio = 1.0 under the zero gravity. In all cases, the calculation grid points of (40×32×40) are employed. Mesh size are unequally distributed in r and z direction. All results described below are obtained by applying a finer time step than that in the last year's report. We calculate three cases. In the case 1, the computation without DSD is performed, while the case 2 is taking the DSD into account. At last in the case 3, we calculate with using increased Ca to investigate the effect of larger free surface deformation. We evaluate the effects of the DSD upon the flow field and critical condition by comparing these cases. In addition, the mutual relationship among the DSD, temperature, pressure and axial velocity is investigated.

4.1.1 Without dynamic free surface deformation

The calculations without dynamic free surface deformation are performed for Re = 900, 1,030, and 1,300 as the case 1. Under the zero gravity, the liquid bridge shape is cylindrical. Figure 5 shows the temperature and velocity distributions. For Re = 900 less than the critical value, the flow becomes axisymmetric steady flow (Fig. 5(a)). Increasing Re up to 1,300 the flow field exhibits the standing-wave oscillation first (Fig. 5(b)), and then changes into the traveling-wave one (Fig. 5(c)). The azimuthal wave number m is mainly determined by the aspect ratio. The relation is indicated as $m\times\Gamma \fallingdotseq 2.2$.[1] The mode number of oscillation is m = 2 in accordance with the structure obtained by the linear stability analysis (LSA). [11] [12]

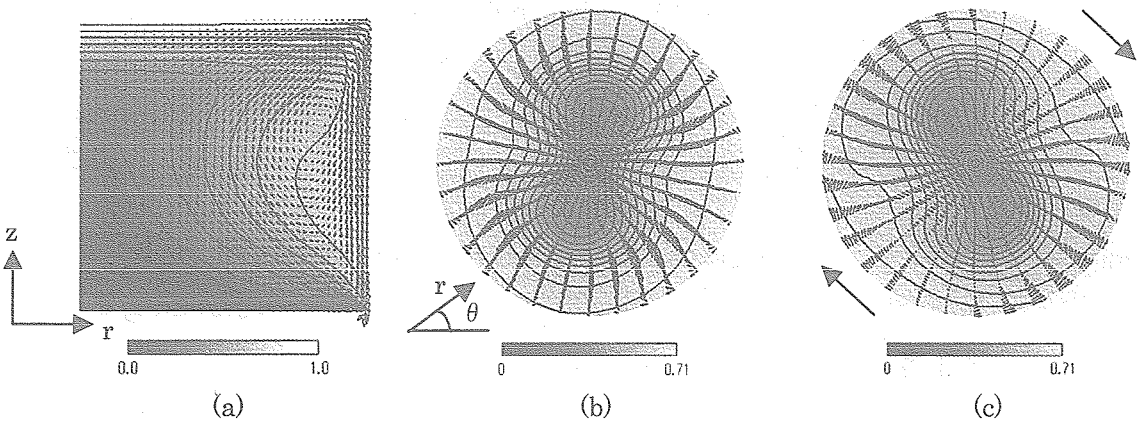

Figure 5: Temperature and velocity distributions in axisymmetric steady flow in r-z place (a), Re = 900, standing wave (b) and traveling wave (c), Re = 1,300 without DSD in r-θ place at mid-height

Figure 6 shows the azimuthal velocity variation on the free surface at mid-height of the liquid bridge. In the case of Re = 900 the azimuthal velocity decreases exponentially, but in the other cases it increases. From this growth rate, we can estimate the critical Reynolds number Re_c (Fig. 6(b)) and compared with the result obtained by LSA for the code validation.

The present calculation gives Re_c = 980. This results is in good agreement with the LSA prediction, Re = 1,013. [4]

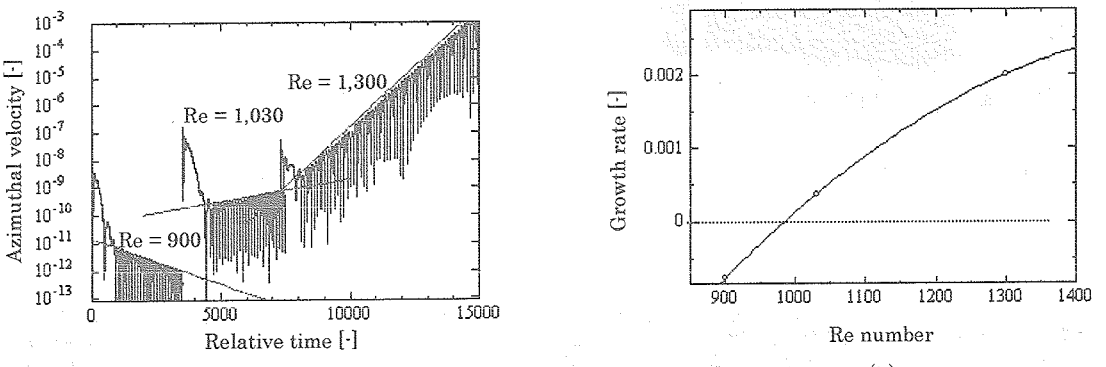

(a) (b)

Figure 6: Azimuthal velocity variations (a) and growth rate (b) for Re = 900～1,300 without DSD

4.1.2 With dynamic free surface deformation

The calculations considering the DSD, as case 2, are performed under the same conditions with the case 1. The Capillary number in the present calculation is assumed to be 0.0027, which corresponds to that of acetone at Re = 1,300. Figure 7 shows the temperature and velocity distributions in axisymmetric steady flow for Re = 900. The free surface shape is shown in Fig. 8. The DSD is quite small. For Re = 1,300 the flow exhibits a transition to the standing wave oscillation first, and changes into traveling wave one like the case 1 (m=2).

The surface deformation is shown in Figure 9. The deformation with the largest amplitude takes place at mid-height of the bridge. The maximum amplitude is about 0.033 μ m for R = 2.5mm. Kawaji et al.[13] found in their experiment that the DSD was too small to be measured, which must be of order 0.1 μ m or less.

Figure 10 shows the azimuthal velocity variations. The critical Reynolds number is estimated to be Re_c = 980, which coincides well with the one calculated without the DSD (case 1). This result also agrees with the one by LSA considering the DSD, Re_c = 951[8]. It is noted that no significant effect of the DSD can be found on the critical condition for the onset of oscillatory flow in spite of the difference of the velocity distributions.

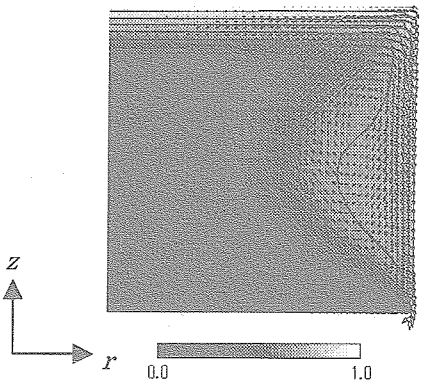

Figure 7: Temperature and velocity distribution for Re = 900 with DSD

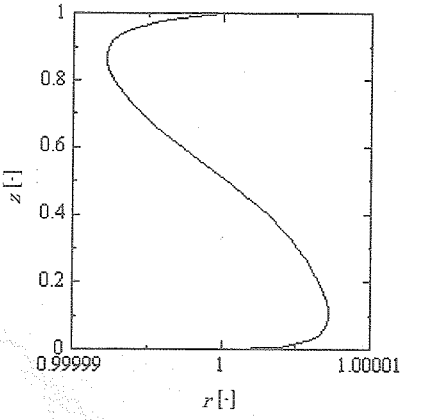

Figure 8: Free surface shape for Re = 900 with DSD

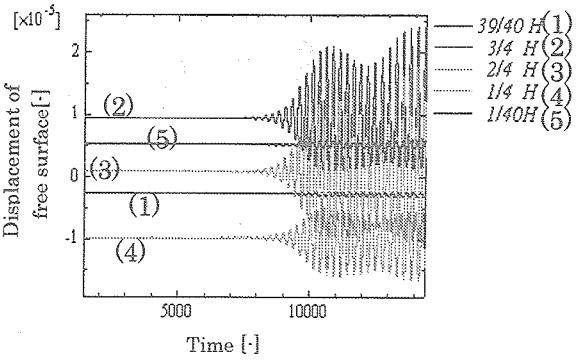

Figure 9: Free surface variation for Re = 1,300

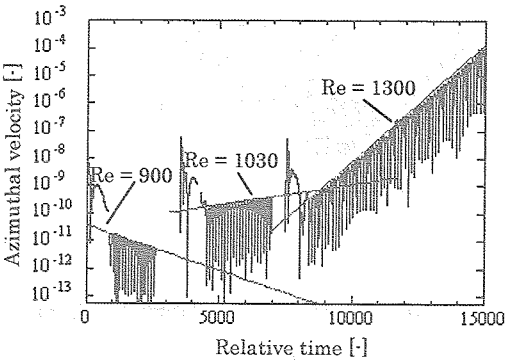

Figure: 10 Azimuthal velocity variation for Re = 900～1,300 with DSD

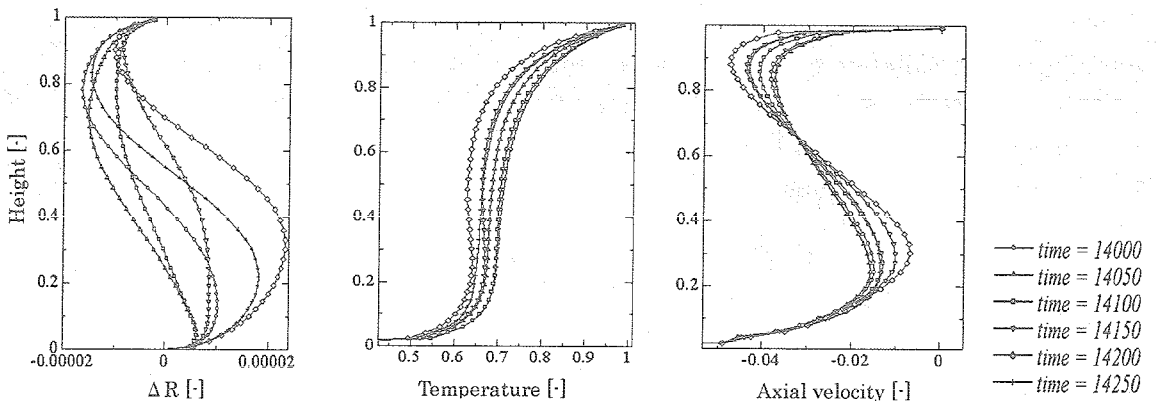

(a) (b) (c)

Figure 11 (a): DSD, (b): surface temperature and (c): axial velocity on the free surface variations of one cycle of traveling wave oscillation.

The capillary number, Ca= $\sigma_T \Delta T / \sigma_0$ is an important non-dimensional parameter for the DSD. Ca = 0 means that the free surface is not deformed dynamically. In order to evaluate the effect of the DSD, we simulate the flow field with a different Ca as the case 3. Here we employ Ca 10 times larger than that in the case 2. Figure 12 shows the free surface shape in the steady flow for Re = 900. The DSD in this case is about 10 times larger than the one with normal Ca, which means the DSD is proportional to Ca. The Re_c estimated by the azimuthal velocity growth rate is Re_c = 1,000 (see Fig. 13) which is a little larger than the case 2 with normal Ca.

It can be considered that the flow is slightly stabilized by the DSD. Here, in the Table 2 the Re_c of three cases are listed.

Table 2: Critical Reynolds numbers of three cases

	Case 1 (without DSD)		Case 2 (with DSD)		Case 3 ($Ca_0 \times 10$)
	Present	LSA [4]	Present	LSA [8]	Present
Re_c	980	1,013	980	951	1,000

Time series of surface deformations and temperature variations for Re = 1,300 in both cases of 2 and 3 are shown in Fig. 14. The onset of the oscillation of the temperature with larger Ca delays in comparison with the case using the normal Ca because of increased critical point.

In qualitatively, however, almost no differences can be seen. There is no striking influence of the DSD on the criticality and flow field in the present conditions.

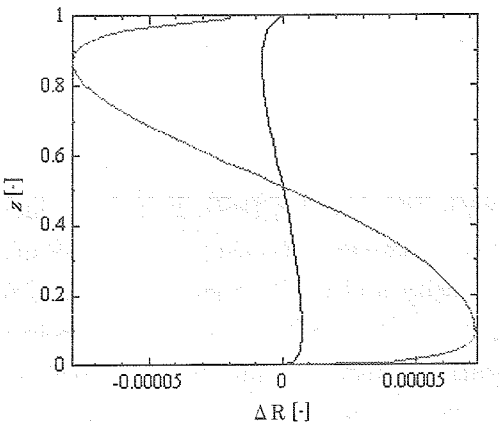

Figure 12: Free surface shape for Re = 900 (black line: $Ca_0 = 2.7 \times 10^3$, gray line: Ca = $Ca_0 \times 10$)

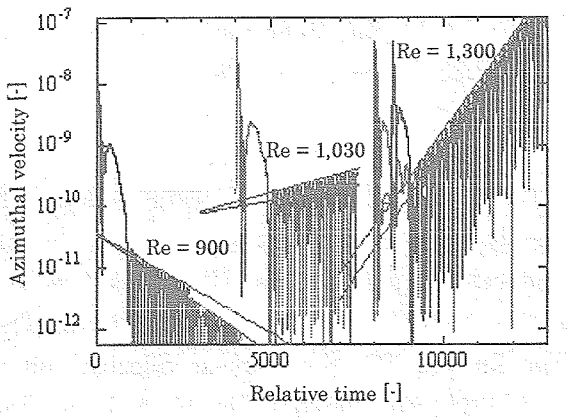

Figure 13: Azimuthal velocity variation (black line: $Ca_0 = 2.7 \times 10^3$, gray line: Ca = $10 \times Ca_0$)

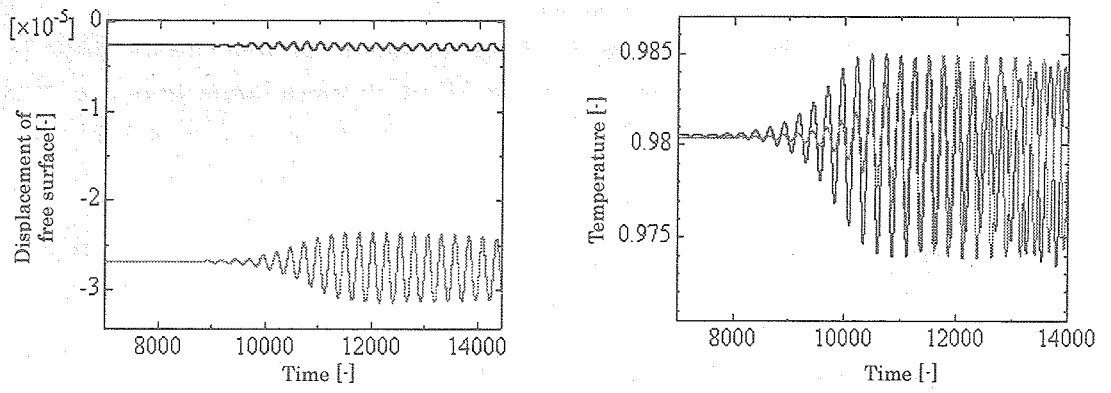

(a) Displacement of free surface and temperature variations near the hot corner (about z = 1/60 from the hot corner)

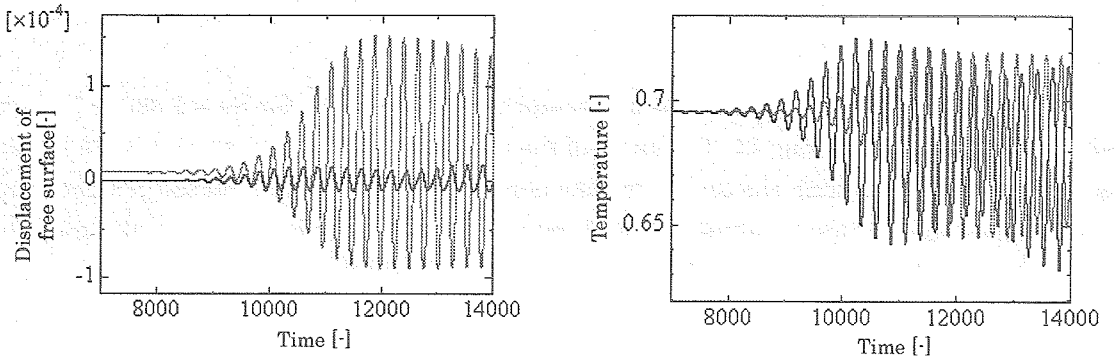

(b) Displacement of free surface and temperature variations at mid-height (z = 1/2H)

Figure 14: Surface deformation and temperature variations for Re = 1,300 (black line: Ca = $Ca_0 = 2.7 \times 10^3$, gray line: Ca = $Ca_0 \times 10$)

Here, we compare the thermal and flow fields with and without DSD. In 2-dimensional steady flow (Re = 900), it is hard to find any differences between both cases from temperature and velocity distributions (Fig. 5(a), Fig. 7). The velocity and the temperature on the free surface in both cases are shown in Fig. 15. The critical conditions of both cases almost coincide. For Re = 1,300, the surface velocity and temperature variations on the free surface at mid-height are shown in Fig. 16. Although the both cases indicate the same critical condition, the growth of the thermal field in the case considering DSD takes longer time than the case without DSD, and thus the onset of the oscillation delays.

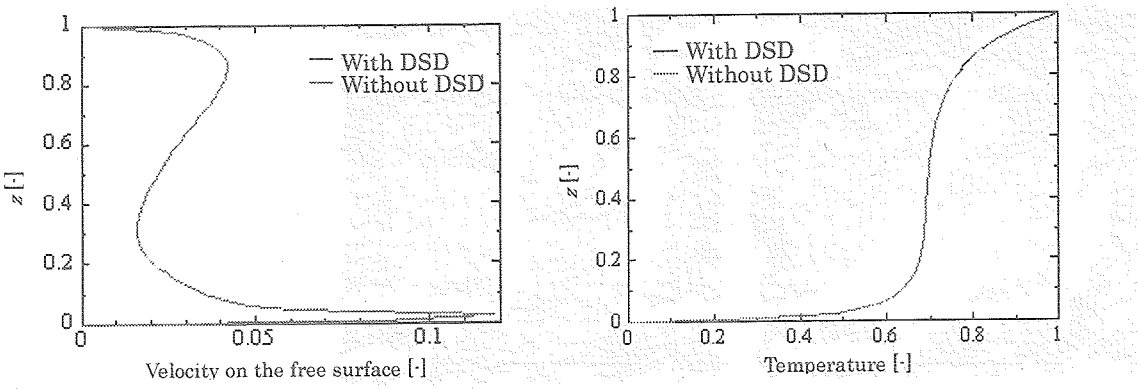

(a) (b)

Figure 15: Absolute velocity (a) and temperature (b) on the free surface for Re = 900.

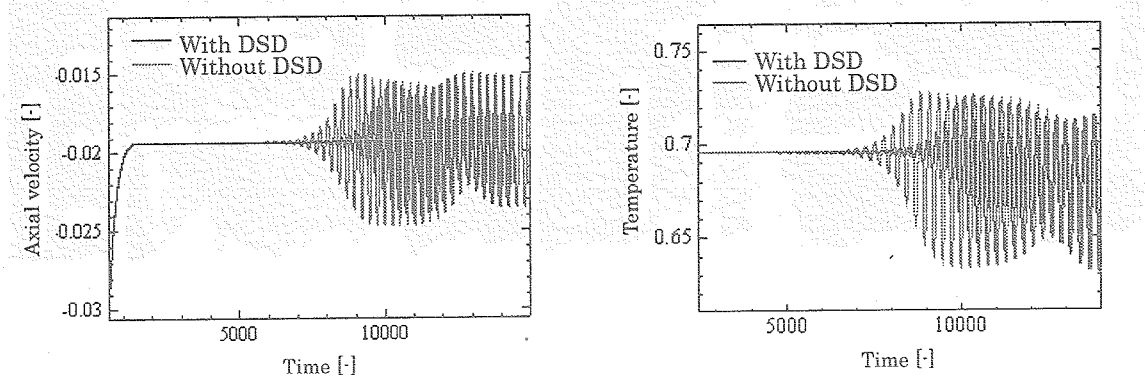

(a) (b)

Figure 16: Axial velocity (a) and temperature (b) variations on the free surface at mid-height of liquid bridge for Re = 1,300 with and without DSD.

Figure 17 shows the mutual relationship among the free surface deformation, temperature and pressure variations. Each variation is the deviation from its mean values. Here, the fluctuation of the free surface displacement from the initial position is magnified 10^4 times because the DSD is quite small. From Figs.17 (a) and (b), it can be found that the low and high temperature regions overlap with the low and high pressure ones, respectively. The same relation also exists between the DSD and the pressure. The free surface is deformed asymmetrically due to the azimuthal rotation in the traveling wave state. That is, the liquid bridge is slightly twisted, and rotates with its shape unchanged. Figure 17(c) shows the snapshot at which low temperature fluid arrives at the free surface near the hot corner.

The fluid near the free surface is then accelerated downward by the Marangoni force, which is enhanced owing to the arrived low-temperature fluid. As the result, a low pressure region is induced near the upper disk (see Fig. 17(d)). As the fluid near the upper disk flows downward, the low pressure region also moves down. Consequently the surface becomes concave due to the low pressure in accordance with the stress balance (see Fig. 17 (e)).

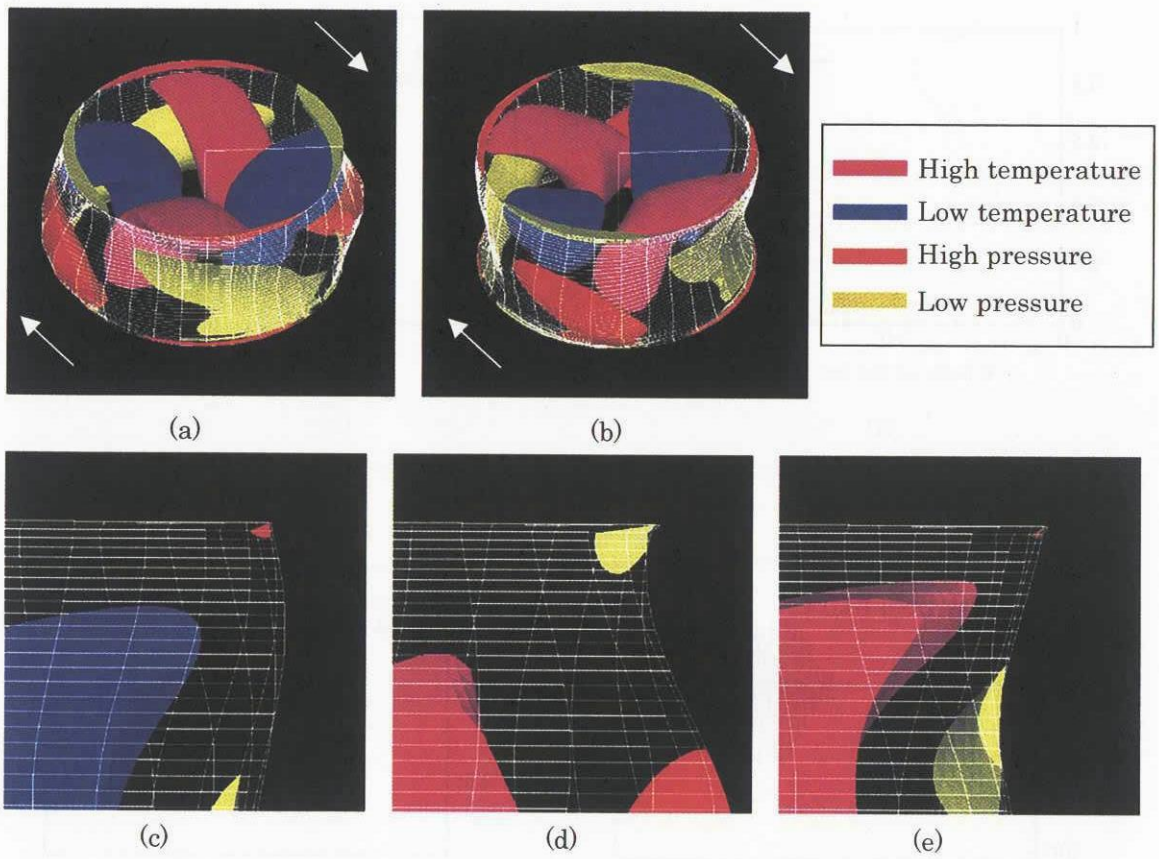

Figure 17: Snapshot of fluctuations of the temperature and pressure. Positive and negative temperature fluctuations are illustrated by purple and blue, respectively. As for pressure, red and yellow, respectively. Frames (a) and (b) represent bird-eye view of those fluctuations; Frames (c)-(e) present the scenario of the surface deformation at the hot corner.

This relation near the hot corner can be indicated from Fig. 18. Figure 18 shows the phase correlation among several quantities at the free surface taken at near the upper and lower disks (about $1/10H$ from each disks), (a) and (c), respectively, and at mid-height ($z = 1/2H$) (b), The variables shown in the figure are the dynamic free surface deformation, the temperature, and the absolute axial velocity in the traveling-wave state. These figures show one cycle of oscillation in the traveling wave state. A phase lag of about $\pi/2$ exists between the temperature difference and the surface deformation near the upper disk. Near the lower disk, on the other hand, the phase difference against the surface velocity and the temperature of the free surface displacement is shifted by π or slightly larger than π. As for the surface deformation, one can conclude that it is mostly determined by the pressure at any axial positions. The non-sinusoidal curves indicate the non-linear character of the oscillation at the computed Reynolds number.

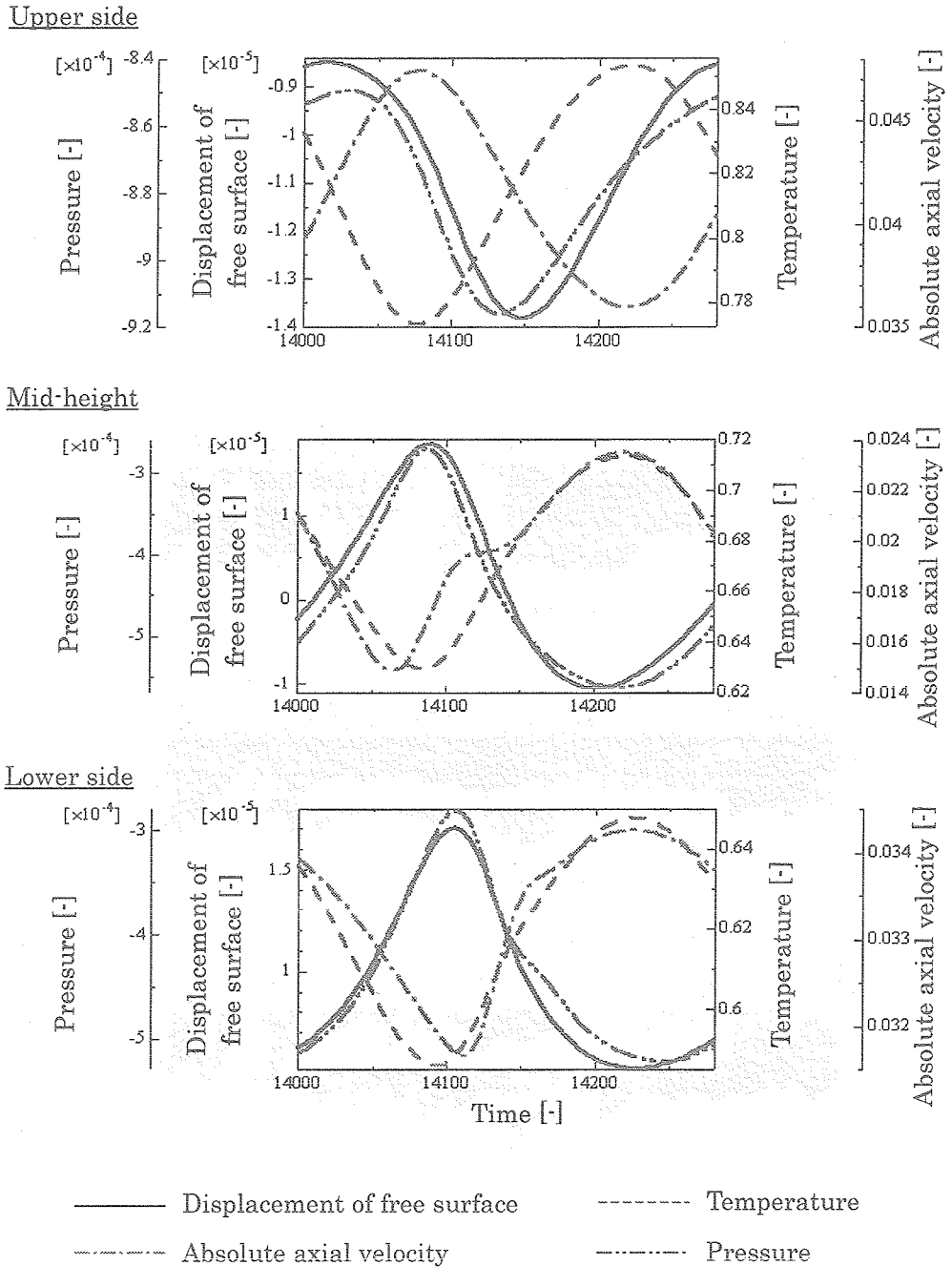

Figure 18: Phase relationship among the surface deformation, pressure, temperature difference and absolute axial velocity in the traveling wave oscillation for Re=1,300.

Figure 19(a) shows the fluctuation of the temperature and the azimuthal component of the velocity over the free surface in the θ-z plane for the traveling wave state, where the wave is advancing in the negative direction of θ. The azimuthal velocity vectors are essentially directed towards the coldest zone. The corresponding radial flow causes the high and low pressure regions (see Fig. 19(b)) and thus results in a surface bulging and receding (Fig. 19(c)).

The concave and convex regions are inclined noticeably against the vertical axis (Fig. 19(c)). The hot temperature region seems to be almost symmetric, while the cold region is distorted near the lower disk (Fig. 19(a)). This distortion causes the inclined pressure distribution and thus the tilted surface deformations. The present relation between the surface deformation and temperature agrees well with that obtained by Kuhlmann et al.[8] using the linear stability analysis.

Almost the entire free surface, the interface recedes at the low temperature region by the influence of the induced high pressure due to the azimuthal Marangoni force.

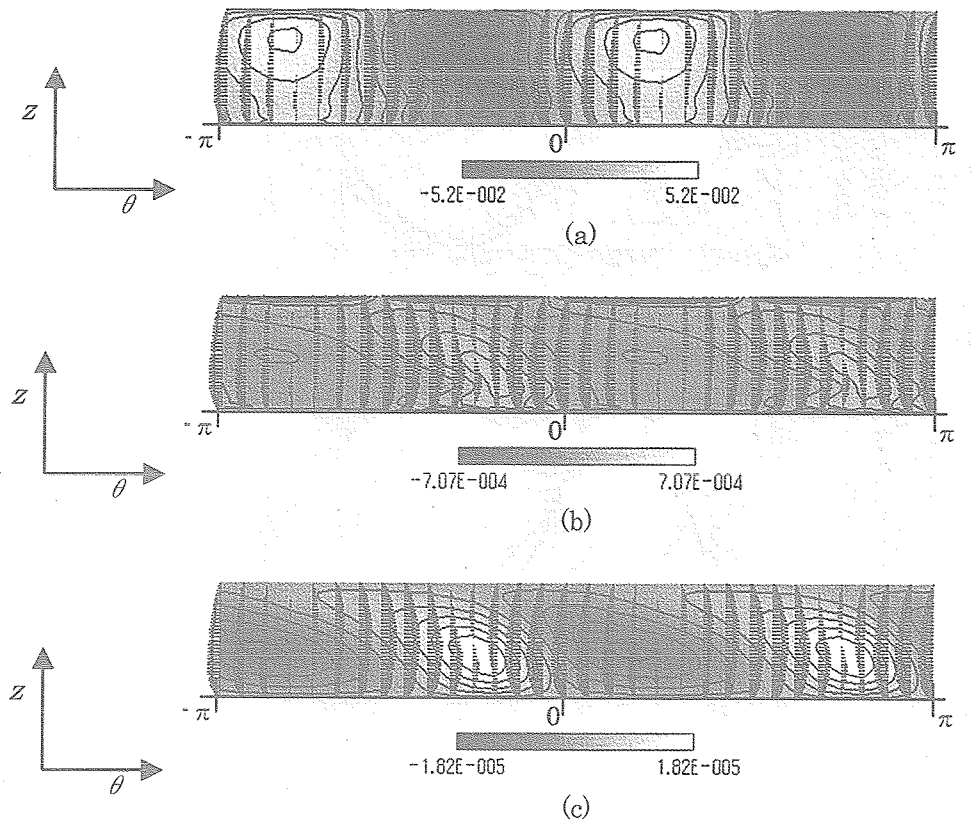

Figure 19: The fluctuations of the (a)temperature, (b)pressure, (c)surface deformation and the azimuthal velocity over the free surface in the traveling wave in θ- z plane for Re = 1,300

4.2 High Pr fluid

Calculation of high Pr fluid needs finer grids in order to resolve the thermal fluid flow with quite thin boundary layer. This means that a large computational time is required, which could be one of the reasons why there exists few work concerning high Pr fluid. We perform the simulation with 2cSt silicone oil (Pr = 28.11), aspect ratio Γ= 1.0 and volume ratio = 1.0 under the zero gravity. The calculation gird points are increased up to ($r\times\theta\times z$) = (56×32×70).

4.2.1 Without dynamic free surface deformation

With uniform-sized coarse mesh, mode number which appears in the bridge is m = 1 in spite of the Γ= 1.0 (the temperature distribution is shown in Fig. 20). Figure 21 shows the temperature distribution on the free surface and at neighboring three grid points in the case of Ma = 20,000. From this temperature distribution, it can be seen that the large temperature gradients for r and z directions exist near the both disks. So, the appearance of different mode number is probably due to the insufficiency of the mesh size. Therefore we use the non-uniform mesh for r and z directions; finer grids are applied in the vicinity of the free surface and in the vicinity of both rods. Widths of the calculation grids (dr, dz) are noted in the Table 3.

Using finer grids, the oscillation of m = 2 is exhibited. The temperature distribution is shown in Fig. 22. The flow field exhibits the standing-wave oscillation first (Fig. 22(b)), and then changes into the traveling-wave one (Fig. 22(c)) at a constant Ma = 40,000, which is the same as the case of acetone. Following results are obtained by using this non-uniform calculation gird (case 4).

Figure 23 shows the azimuthal velocity variation. The estimated critical Marangoni number is $Ma_c \fallingdotseq$ 32,500. In the experiment, the Ma_c is less than 20,000[14], which is smaller compared with the Ma_c obtained by the present calculation.

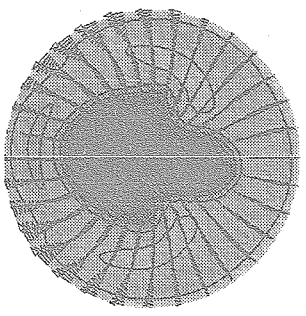

Figure 20: Temperature and velocity distributions for Ma = 35,000 without DSD in r-θ plane at mid-height

Table 3: Widths of the grids

	uniform mesh	non-uniform mesh
dr (r-direction)	1.8×10^{-2}	6.1×10^{-3} (dr_{min})
dz (z-direction)	1.4×10^{-2}	7.7×10^{-3} (dz_{min})

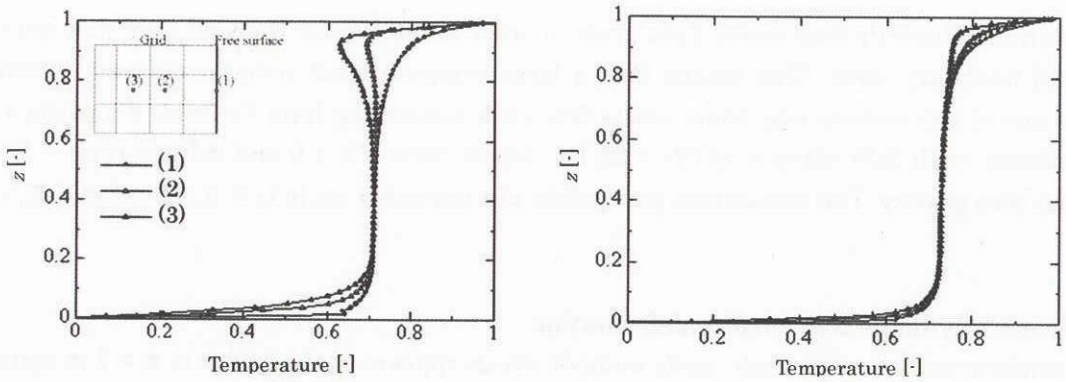

Figure 21: Temperature distribution on the free surface at neighboring three grid points for Ma = 20,000; (a) Using uniform grid, (b) Using non-uniform grid

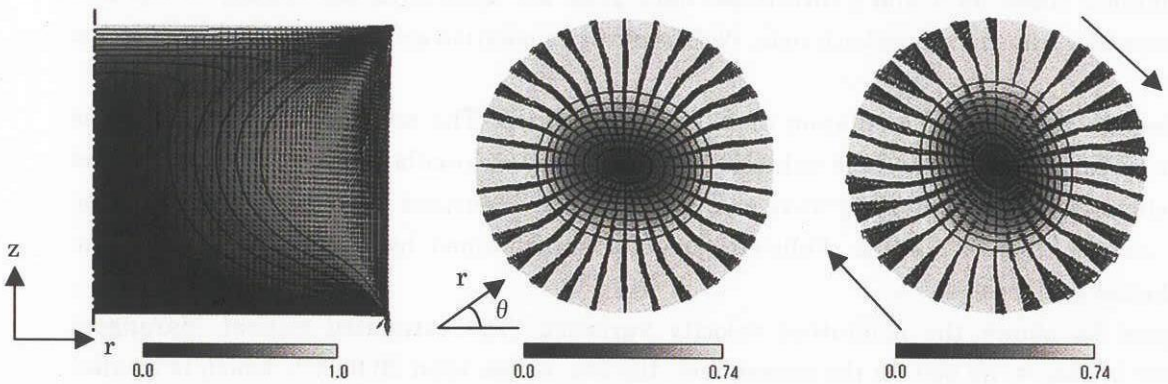

Figure 22: Temperature and velocity distributions in axisymmetric steady flow in r - z place (a) for Ma = 20,000, standing wave (b) and traveling wave (c) for Ma = 40,000 without DSD in r - θ place at mid-height

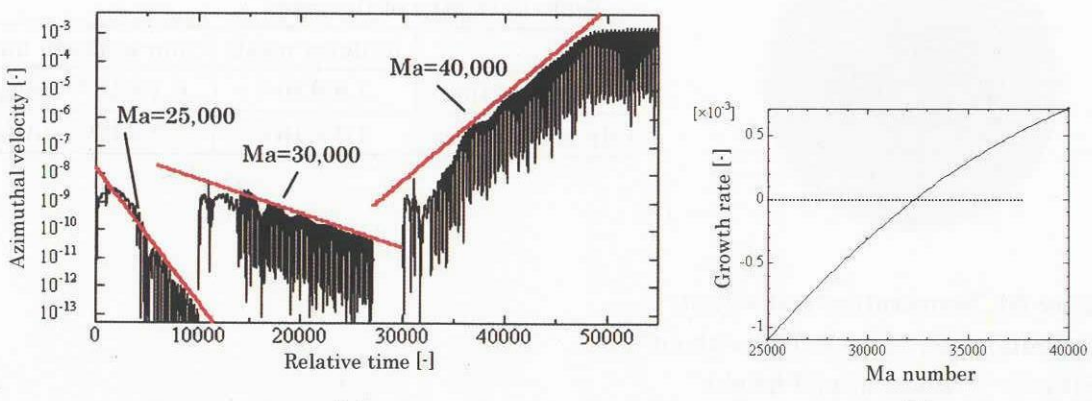

Figure 23: (a) Azimuthal velocity variation and (b) growth rate without DSD for Ma = 25,000～40,000

Figure 24 shows the azimuthal velocity and the temperature variations at mid-height for Ma = 40,000. The black line indicates the value at $\theta = 1/4\,\pi$, which corresponds to the node point of the temperature and anti-node point of the azimuthal velocity in the standing wave oscillation. On the other hand, the gray line indicates the value at $\theta = 0$, the anti-node point of the temperature and node point of the azimuthal velocity. From this figure, the flow exhibits the standing wave flow at the early stage of the oscillation. But the temperature and the azimuthal velocity of the node point is not stable and keeps increasing gradually. After all, the amplitudes of black and gray lines coincide, and the flow exhibits the traveling wave oscillation. Therefore it can be said that the standing wave oscillation in the present condition is not fully stable and is the transition state for the traveling one.

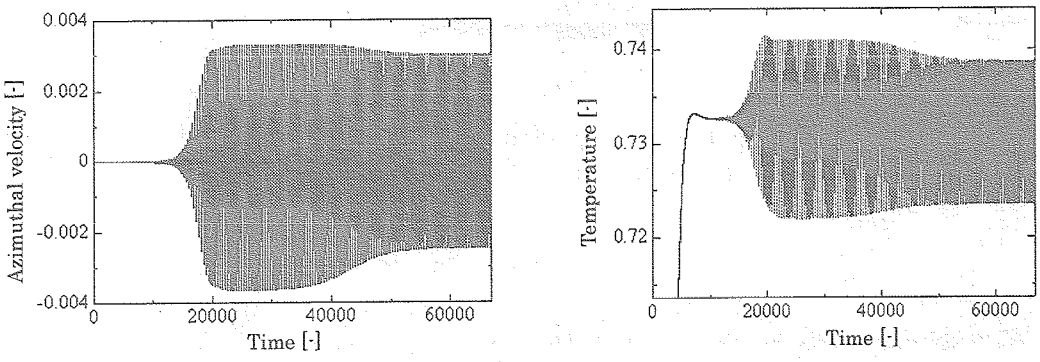

(a) (b)

Figure 24: (a) Azimuthal velocity and (b) temperature variations at mid-height for Ma = 40,000 (black: $\theta = 1/4\,\pi$, gray: $\theta = 0$)

Figure 25 shows the fluctuations of the temperature, the pressure and the azimuthal component of the velocity over the free surface in θ-z plane for the traveling wave state, where the wave is advancing in the negative direction of θ. Like the cases 1 and 2, the azimuthal velocity vectors are mostly directed towards the coldest zone. The fluctuation of the temperature indicates, on the other hand, meandering distribution at $z \fallingdotseq 1/4H$, which is different from the case of acetone. The fluctuation of the pressure also indicates the meandering distribution.

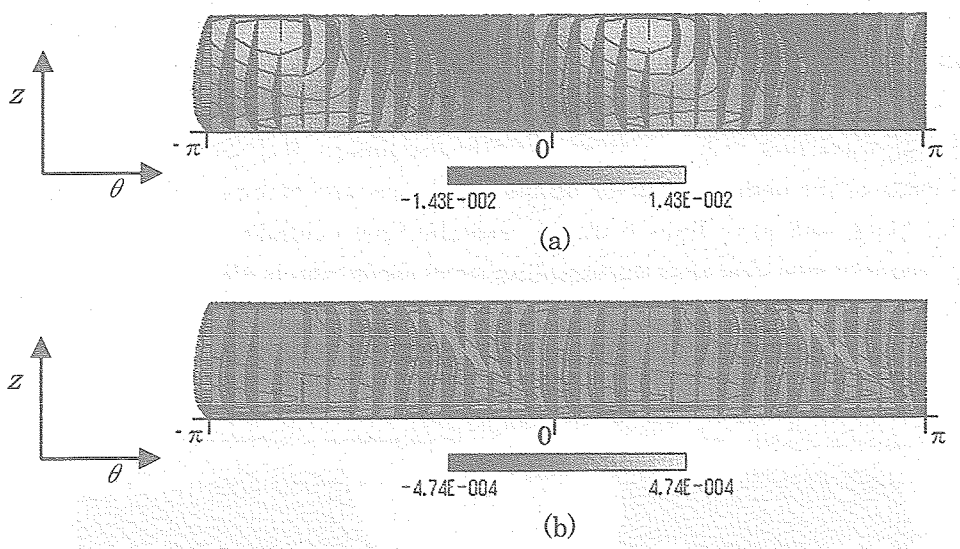

Figure 25: The fluctuations of the (a)temperature, (b)pressure and the azimuthal velocity over the free surface in the traveling wave in θ - z plane for Ma=40,000

4. 4. 2 With dynamic free surface deformation

The calculation with DSD as the case 5 is performed for Ma = 20,000～25,000. The capillary number is assumed to be 0.068, which corresponds to the one for 2cSt silicone oil at Ma = 25,000. The calculation is started with the cylindrical shape because of the zero gravity. Figure 26 shows the temperature and the velocity distributions in the axisymmetric steady flow for Ma = 20,000. The surface displacement is shown in Fig. 27. The maximum free surface displacement is about 0.38 μ m for R = 2.5mm.

Figure 28 shows the azimuthal velocity variation for Ma = 20,000 and 25,000. In the present results, the calculations are carried out for two different Ma. Therefore, it is rather hard to estimate Ma_c. The growth of the azimuthal velocity between the case 4 and 5 almost coincide for Ma = 20,000. For Ma = 25,000, the growth rate of the azimuthal velocity with DSD is little larger than the one without DSD. Therefore, it can be estimated that the Ma_c with DSD is less than Ma = 32,500.

The velocity and the temperature distributions on the free surface with and without DSD for Ma = 20,000 are shown in Fig. 29. Comparison between the case 4 and case 5 indicates that both the velocity and the temperature distributions show no significant differences.

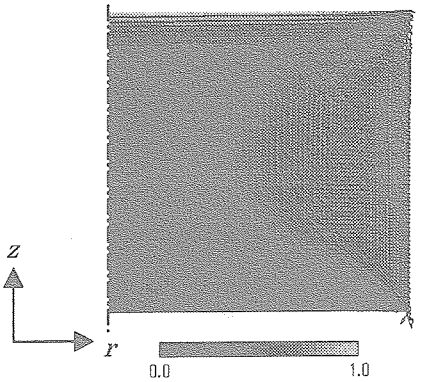

Figure 26: Temperature and velocity distributions for Ma = 20,000 in r - z plane

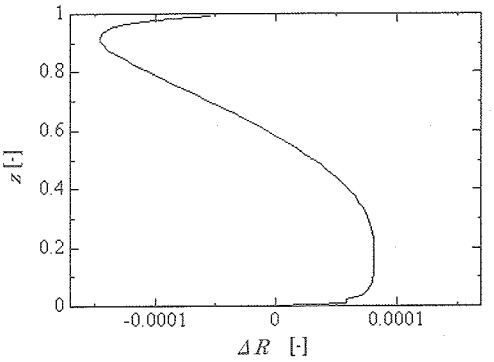

Figure 27: Free surface shape for Ma = 20,000 with DSD

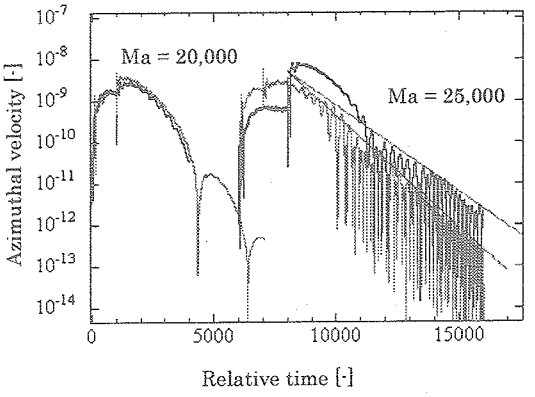

Figure 28: Azimuthal velocity variation for Ma = 20,000 and 25,000 (black: with DSD, gray: without DSD)

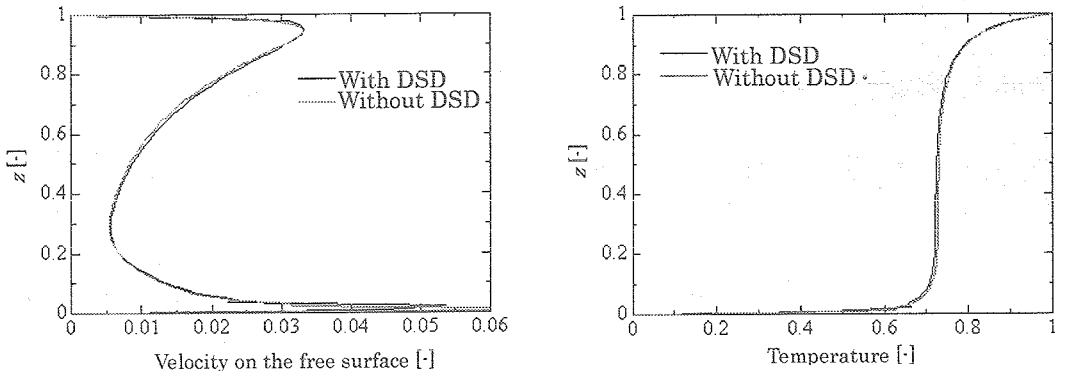

(a) (b)

Figure 29: Absolute velocity (a) and temperature (b) on the free surface for Ma = 20,000

The surface deformation in the oscillatory flow is not obtained in present calculations because of the shortage of the calculation time. From the fluctuation of the temperature and pressure over the free surface of the case 4 (Fig. 25) it can be considered that the surface deformation also indicates meandering distribution.

5 CONCLUSIONS

5.1 Medium Pr fluid acetone (Pr = 4.38)

(1) The thermocapillary convection with dynamic free surface deformation is calculated successfully.

(2) The obtained critical Reynolds number $Re_c = 980$ is in good agreement with the results of the linear stability analysis.

(3) Effect of the DSD upon the Re_c and the flow field is not seen clearly in the range of present numerical simulation.

(4) Mutual relation among the DSD, the temperature, the pressure and the axial velocity is obtained.

(5) Increasing the capillary number ($Ca = 10 \times Ca_0$), the Re_c estimated 1,000 was little higher than normal condition, but we found almost no qualitative differences in the flow field.

5.2 High Pr fluid 2cSt silicone oil (Pr = 28.11)

(1) Using finer grids, the oscillation of $m = 2$ is obtained in the case without DSD.

(2) The critical Marangoni number in the case without DSD is obtained. The Ma_c is higher than the one obtained by the experiment.

(3) The fluctuation of the temperature and the pressure over the free surface indicate meandering distribution, which is different from the case of the medium Pr fluid acetone.

(4) The Ma_c in the case with DSD is estimated smaller than the one without DSD.

(5) In the axisymmetric steady flow, there are no significant difference between the cases with and without DSD from the temperature and the velocity distributions on the free surface.

6 REFERENCES

[1] Preisser, F., Schwabe, D. and Scharmann, A., 1983, Steady and oscillatory thermocapillary convection in liquid bridge columns with free cylindrical surface. J. Fluid Mech. 126, 545-567.

[2] Velten, R., Schwabe, D. and Scharmann, A., 1991, The periodic instability of thermocapillary convection in cylindrical liquid bridges. Phys. Fluids A3 (2), 267-279.

[3] Kuhlmann, H. C. and Rath, H. J., 1993, Hydrodynamic instabilities in cylindrical thermocapillary liquid bridges. J. Fluid Mech. 247, 247-274.

[4] Wanschura, M., Shevtsova, V. M., Kuhlmann, H. C. and Rath, H. J., 1995, Convective instability mechanisms in thermocapillary liquid bridges, Phys. Fluids 7,912.

[5] Savino, R. and Monti, R., 1996, Oscillatory Marangoni convection in cylindrical liquid bridges. Phys. Fluids 8, 2906-2922.

[6] Shevtsova, V. M. and Legros, J. C., 1998, Oscillatory convective motion in deformed liquid bridges. Phys. Fluids 10, 1621-1634.

[7] Kamotani, Y., Ostrach, S. and Masud, J., 2000, Microgravity experiments and analysis of oscillatory thermocapillary flows in cylindrical containers. J. Fluid Mech. 410, 211-233.

[8] Kuhlmann, H. C. and Nienhüser, C., 2002, Dynamic free-surface deformations in thermocapillary liquid bridge, Fluid Dynamics Research 31, 103 (2002).

[9] Kuhlmann, H. C., 1999, Thermocapillary Convection in Models of Crystal Growth. Springer, pp.11-18.

[10] Goto, M., Shida, K., Ueno, I., Kawamura, H. and Yoda, S., 2001, Numerical Simulation of Marangoni Convection in Consideration of Free Surface Displacement (Part 4). Marangoni Convection Modeling Research Annual Report.

[11] Leypoldt, J., Kuhlmann, H. C. and Rath, H. J., 2000, Three-dimensional numerical simulation of thermocapillary flows in cylindrical liquid bridges. J. Fluid Mech. 414, 285-314.

[12] Kawamura, H., Ueno, I. and Ishikawa, T., Study of Thermocapillary Flow in a Liquid Bridge towards an On-Orbit Experiment aboard the International Space Station. Advances in Space Research, accepted to appear

[13] Kawaji, M., Otsubo, F., Simic, S. and Yoda, S., 2000, Transition to Oscillatory Marangoni Convection in Liquid Bridges of Intermediate Prandtl Number. Marangoni Convection Modeling Research Annual Report.

[14] Ueno, I., Ono, Y., Nagano, D., Tanaka, S. and Kawamura, H., 2000, Modal Oscillatory Structure and Dynamic Particle Accumulation in Liquid Bridge Marangoni Convection, Proc. 4th JSME-KSME Thermal Eng. Conf., Vol.3, pp.265-270.